



Mapping ground displacement by a multiple phase difference-based InSAR approach: with stochastic model estimation and turbulent troposphere mitigation

Yunmeng Cao^{1,2} · Zhiwei Li¹ · Falk Amelung²

Received: 24 September 2018 / Accepted: 28 February 2019 / Published online: 9 March 2019
© Springer-Verlag GmbH Germany, part of Springer Nature 2019

Abstract

Tropospheric delay is one of the dominant error sources of interferometric synthetic aperture radar when measuring ground displacement. Although many methods have been presented for the correction of tropospheric effects, a large portion of them (such as the numerical weather models and the topography-correlated analysis methods) can only be used to correct the stratified delays (i.e., topography-related delays), and it is still intractable for mitigating the turbulent effects. Considering that the approximate displacement extent over an interested region often can be known based on some prior geophysical or geological information, we present here a new method to mitigate the effects of atmospheric turbulence by fusing multiple phase differences (MPDs) between the pixel of interest and those pixels whose displacement can be ignored or can be known based on external displacement datasets (e.g., from other geodetic observations). Our method involves estimating the stochastic model, i.e., variance–covariance matrix, of the MPDs for each pixel and then reconstructing the ground displacement pixel by pixel using a proposed minimum variance-based linear estimator. Two advantages of the proposed method are that: (1) no external atmospheric data are required; (2) uncertainties of the reconstructed displacements can be provided as well. In addition, our method is implemented interferogram by interferogram, so we do not need time series of InSAR datasets. The performance of the proposed approach is tested by using both simulated datasets and the real data over Mexico City regions, and the experimental results show that our method can mitigate the turbulent atmosphere efficiently and robustly, which is of great interest to a wide community of geodesists and geophysicists.

Keywords Interferometric synthetic aperture radar (InSAR) · Atmosphere correction · Turbulent troposphere mitigation · Minimum variance estimator

1 Introduction

Interferometric synthetic aperture radar (SAR) (InSAR) has been proved to be a powerful technology for measuring ground surface displacement with wide spatial coverage, high spatial resolution, and all-weather and day-and-night working capability (Massonnet and Feigl 1998; Lu et al. 2007; Chen et al. 2017). Although significant progresses have been made in the past two decades to improve the

measurement precision, the tropospheric delays (i.e., the radar propagation error due to neutral atmosphere), which is mainly caused by the variation of temperature, pressure, and relative humidity both in time and in space, still remain one of the dominate error sources for accurately measuring the ground displacements (Zebker et al. 1997; Hanssen 2001; Ding et al. 2008; Kinoshita et al. 2012; Cao et al. 2017).

The tropospheric delays can be separated into the stratified and the turbulent components in the spatial domain, based on their physical origin (Hanssen 2001). Many methods have been presented for the correction of tropospheric effects; however, a large portion of them can only be used to correct the effects of stratified atmosphere, like the numerical weather model-based methods (Foster et al. 2006; Jolivet et al. 2011, 2014) and the topography-correlated analysis algorithms (Elliott et al. 2008; Lin et al. 2010; Xu et al. 2011; Bekaert et al. 2015). External water vapor dataset (like MERIS/MODIS- and

✉ Zhiwei Li
zwli@csu.edu.cn

¹ School of Geoscience and Info-Physics, Central South University, Changsha, Hunan, China

² Rosenstiel School of Marine and Atmospheric Science, University of Miami, Miami, USA

GPS-based water vapor dataset)-based methods can be used to theoretically mitigate the total effects of troposphere (both stratified and turbulent atmospheres), while the mapping of the delay from zenith to radar LOS (line of sight) is based on the assumption that there are no heterogeneities within the horizontal layers (Onn 2006), which is in conflict with the spatial heterogeneity characteristic of the turbulent atmosphere. In addition, GPS-based correction is often limited by the low spatial density of the stations (Li et al. 2004), and the MERIS/MODIS satellites only work during daytime and their measurements can be easily polluted by cloud (Li 2005). Time-series InSAR (TS-InSAR)-based filtering methods are another type of choice for the correction of the turbulent atmosphere (Ferretti et al. 2001; Berardino et al. 2002; Hooper 2008), but determination of the filtering window length and the weighting strategy is not straightforward due to the fact that the turbulent atmospheric delay is usually not Gaussian-distributed in the temporal domain (Gong et al. 2015; Cao et al. 2017). Therefore, how to correct the effects of turbulent atmosphere is still an intractable problem.

In this paper, we present a new method to mitigate the effects of turbulent atmosphere by fully exploiting those available displacement-known pixels (i.e., pixels with known displacement or within non-deforming area). Our method aims to mitigate the turbulent effects by fusing multiple phase differences (MPDs) between the pixel of interest and the pixels with displacement known, including those pixels: (i) located in a stable, non-deforming area, or (ii) with displacements known from other geodetic observations. The three steps of the method are: (i) to model the spatial variation of the turbulent atmosphere field by estimating its structure function; (ii) to estimate the stochastic model, i.e., variance–covariance matrix (VCM), of the MPDs for each pixel; and (iii) to reconstruct the ground displacement pixel by pixel using a novel minimum variance-based linear estimator. The method provides the uncertainties of the reconstructed displacements as well. It is implemented interferogram by interferogram and does not need time series of InSAR datasets.

The paper is structured as follows: In Sect. 2, we introduce the proposed new method in detail. The performance of our new method is tested by using both the simulated datasets and the real Sentinel-1A data over Mexico City region in Sects. 3 and 4, respectively. In Sect. 5, we discuss the influences of some factors on the new method, and finally in Sect. 6, we draw our conclusions and provide some outlooks.

2 Methodology

In this section, we propose a new method to mitigate the turbulent atmospheric delays in an interferogram of interest. As to the possible stratified atmospheric delays (i.e.,

topography-related atmosphere), we present to correct this part of delays by firstly modeling the mathematical relationship between the InSAR observations and the related elevations from an external DEM, based on the well-studied Onn model (Onn and Zebker 2006; Xu et al. 2011), and then removing the modeled stratified components from the original InSAR observations. In order to weaken the effects of possible deformations and decorrelation noises for modeling the stratified delays, we recommend masking those significantly deforming and lowly coherent areas when best-fitting the model parameters. In the following analysis, we assume that the stratified atmosphere has been corrected, and consider that the major components of the atmospheric delays in the interferogram of interest are the turbulent delays.

2.1 Definition of multiple phase differences

We consider that n displacement-known pixels have been selected from the whole interferogram; then, we can get n phase differences for an interested pixel p within unknown deformation area, and we write each phase difference as the sum of three terms: (1) displacement, (2) spatial correlated component, and (3) the spatial independent term

$$\varphi_p(r_i) = -\frac{4\pi}{\lambda} [(d_p - d_{r_i}) + (s_p - s_{r_i}) + (e_p - e_{r_i})], \quad i = 1, 2, \dots, n \quad (1)$$

where $\varphi_p(r_i)$ is the phase difference between the interested pixel p and the i th displacement-known pixel r_i ; d_p and d_{r_i} represent the LOS displacements at pixel p and the pixel r_i , respectively, that d_p is the primary interested parameter that we need to estimate and d_{r_i} can be obtained from the prior displacement information (equals zero or can be derived from external displacement datasets); s_p and s_{r_i} account for the spatially correlated components at the two pixels, respectively, which should be mainly associated with the atmospheric delays; and e_p and e_{r_i} denote the spatially independent noises at the two pixels, which is mainly related to the spatial and temporal decorrelation noises. We illustrate the n MPDs of pixel p as Fig. 1.

2.2 Error analysis of multiple phase differences

As the only parameter of interest in our research is the displacement d_p , here we refer to other components in the phase difference as errors. Based on each phase difference, we can get an approximate displacement for the pixel of interest

$$\hat{d}_p(r_i) = -\frac{\lambda}{4\pi} \varphi_p(r_i) + d_{r_i} = d_p + \varepsilon_p(r_i), \quad i = 1, 2, \dots, n \quad (2)$$

where $\varepsilon_p(r_i)$ means the estimation error of $\hat{d}_p(r_i)$ (i.e., the difference between $\hat{d}_p(r_i)$ and d_p). By using n MPDs, we can get n approximate values of the displacement d_p , and the

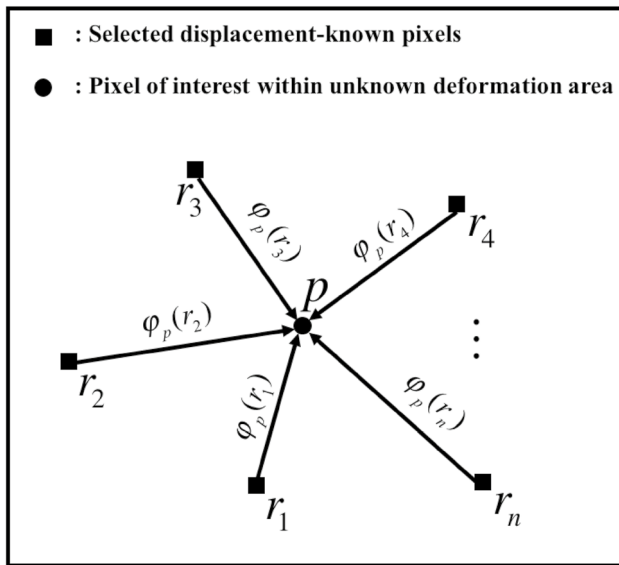


Fig. 1 Illustration of multiple phase differences (MPDs)

vector of the n approximate displacements at pixel p can be written as $L_p = [\hat{d}_p(r_1), \hat{d}_p(r_2), \dots, \hat{d}_p(r_n)]^T$. From Eq. (1) and Eq. (2), we can find that $\varepsilon_p(r_i)$ can be presented as:

$$\varepsilon_p(r_i) = \Delta d_{r_i} + (s_p - s_{r_i}) + (e_p - e_{r_i}) \quad (3)$$

where Δd_{r_i} accounts for the prior displacement error of the i th displacement-known pixel, and it is caused by the inconsistency between the real displacement phase in InSAR at pixel r_i and the arbitrary displacement value (which is assumed to be zero or derived from external displacement datasets). This inconsistency can be related to two facts: firstly, absolutely non-deforming is not possible in reality; thus, the selected displacement-known pixels in the so-called non-deforming areas are usually deformed to some degree, even the deforming magnitudes could be very small; secondly, other geodetic techniques derived displacements are always not equal to the real displacements in InSAR, due to the uncertainty of the external dataset itself and the intrinsic differences between InSAR and other geodetic techniques, for example InSAR displacement usually means an average value of the whole pixel (e.g., $20 \text{ m} \times 20 \text{ m}$), while pointwise displacement of GPS or leveling is associated with one geometrical ground point. For the spatial correlated errors, here we consider that it is mainly caused by the effect of turbulent atmosphere, as we assume that the stratified atmosphere can be corrected by using weather models (Jolivet et al. 2014) or topography correlation methods (Xu et al. 2011; Bekaert et al. 2015), and we also do not consider the effects of ionosphere in this research. As to the spatial independent noises, we simply take it as the decorrelation noise in our following analysis.

2.3 Stochastic modeling for multiple phase differences

Considering that (i) different phase differences derived displacements (Eq. 2) could have different uncertainties (i.e., qualities); (ii) the n approximate displacements that derived from MPDs are correlated with each other, in this section, we estimate the stochastic model, i.e., variance–covariance matrix (VCM), of the MPDs to provide a reasonable weighting strategy for fusing the n MPDs.

As the three error terms in Eq. (3) can be considered to be independent, we can write the variance of the i th MPD-derived displacement as

$$\sigma_{d_p}^2(r_i) = \text{Var}(\Delta d_{r_i}) + \text{Var}(s_p - s_{r_i}) + \text{Var}(e_p - e_{r_i}) \quad (4)$$

where $\text{Var}(\cdot)$ represents the operation of evaluating the variance, $\sigma_{d_p}^2(r_i)$ represents the variance of the i th MPD-based displacement ($\hat{d}_p(r_i)$), and the covariance between the i th and the j th MPD-derived displacements ($\hat{d}_p(r_i)$ and $\hat{d}_p(r_j)$) can be written as:

$$\begin{aligned} \sigma_{d_p}^2(r_i, r_j) = & \text{Cov}(\Delta d_{r_i}, \Delta d_{r_j}) + \text{Cov}[(s_p - s_{r_i})(s_p - s_{r_j})] \\ & + \text{Cov}[(e_p - e_{r_i})(e_p - e_{r_j})] \end{aligned} \quad (5)$$

where $\text{Cov}(\cdot)$ denote the operation of estimating the covariance; $\sigma_{d_p}^2(r_i, r_j)$ accounts for the covariance between $\hat{d}_p(r_i)$ and $\hat{d}_p(r_j)$. In order to estimate the above variance–covariance components ($\sigma_{d_p}^2(r_i)$ and $\sigma_{d_p}^2(r_i, r_j)$), we should estimate the variance of each component, respectively.

As to the stochastic model of the prior displacement error (Δd_{r_i}), it is quite difficult to model in a routine mathematical way in practice. Therefore, we will not consider the stochastic model of this part in the following analysis; instead, we would analyze the effects of these errors in the discussion part (see Sect. 5.3). Here we would focus on stochastic modeling for the turbulent atmospheric delays and the decorrelation noises.

2.3.1 Variance–covariance components estimation for the turbulent atmospheric delays

The spatial variation characteristic of atmospheric delay (i.e., spatially related noises) has been systematically studied in the previous researches (Hanssen 2001; Emaradson et al. 2003; Knospe and Jónsson 2010; Cao et al. 2014, 2017). The intrinsic hypothesis, which assumes the variance and the expectation are constant for each realization of the random field, is commonly used to estimate the structure function (i.e., spatial variance model) (Cressie 1990; Hanssen 2001). In addition, according to the spatial variation characteristic

of atmospheric delay, we can divide the variation into isotropy and anisotropy (Knospe and Jónsson 2010; Cao et al. 2014). Isotropy means magnitude of the variance only depends on the distance between two pixels, while anisotropy implies that the variance is related to both the distance and the direction (i.e., angle of the line between two pixels). Here we estimate the variance–covariance components of the turbulent atmosphere [see Eqs. (4) and (5)] based on the intrinsic isotropic hypothesis. The variance of InSAR atmospheric delays can be represented by Hanssen (2001) and Emaradson et al. (2003)

$$\text{Var}(s_p - s_{r_i}) = \sigma_{d_p}^2(r_i) = E\left[\left(s(x) - s(x + h_{p,r_i})\right)^2\right] \quad (6)$$

where h_{p,r_i} means the distance between the interested pixel and the i th displacement-known pixel; $s(x)$ represents the magnitude of the turbulent atmospheric delay at position x ; $(x, x + h_{p,r_i})$ accounts for any of the two location pairs, where the distance between them is h_{p,r_i} ; and $E[\cdot]$ is the operation of evaluating the expectation value, which we can estimate it by averaging all of the computed samples. There are several empirical models that can be used to estimate the structure function, such as the Matérn covariance model (Knospe and Jónsson 2010), the spherical model (Cressie 1990; Xu et al. 2011; Cao et al. 2017), and the Bessel-type functional model (González and Fernández 2011). In our previous research (Cao et al. 2017), the spherical model was shown to be adequate for modeling the atmosphere structure function, so we choose it again here as our candidate model. Based on the computed variance samples from Eq. (6), we can determine the best-fit parameters (nugget, rang, and sill) of the spherical model (or any other used model). Let us define the best-fitted structure function as $\gamma(h)$; then, we can get the variance of atmospheric delay (that between pixel r_i and p) (Onn and Zebker 2006; Sudhaus and Jónsson 2009):

$$\text{Var}(s_p - s_{r_i}) = \gamma(h_{p,r_i}) \quad (7)$$

According to the variance–covariance propagation theory and the intrinsic hypothesis, the covariance of the atmospheric delay in Eq. (5) can be written as:

$$\begin{aligned} \text{Cov}\left[(s_p - s_{r_i})(s_p - s_{r_j})\right] &= \text{Cov}(s_p, s_p) + \text{Cov}(s_p, s_{r_i}) + \text{Cov}(s_p, s_{r_j}) + \text{Cov}(s_{r_i}, s_{r_j}) \\ &= \frac{1}{2}\left[\text{Var}(s_p - s_{r_i}) + \text{Var}(s_p - s_{r_j}) - \text{Var}(s_{r_i} - s_{r_j})\right] \end{aligned} \quad (8)$$

Based on the estimated structure function $\gamma(h)$, we can obtain:

$$\text{Cov}\left[(s_p - s_{r_i})(s_p - s_{r_j})\right] = \frac{1}{2}\left[\gamma(h_{p,r_i}) + \gamma(h_{p,r_j}) - \gamma(h_{r_i,r_j})\right] \quad (9)$$

It is easy to find that the covariance of the two different MPD-based turbulent atmospheric delays (see Eq. (9)) is determined by the spatial geometry (i.e., triangular) of the three positions (the two displacement-known pixels and the pixel of interest).

2.3.2 Spatial variance–covariance estimation of the decorrelation noises

The decorrelation noise of the interferometric phase is composed of temporal decorrelation that is caused by the change in surface scattering properties over time, spatial decorrelation (i.e., geometric decorrelation), spectral misalignment due to the two different imaging positions of the satellite, and radar receiver thermal noise (Zebker and Villasenor 1992; Bamler and Hartl 1998). A common way to model the variance of decorrelation noises is by using the coherence value (between 0 and 1) and the multi-look numbers of the interferometric phase (Rodríguez and Martín 1992; Bamler and Hartl 1998; Hanssen 2001; Li et al. 2008). Because we also consider that the decorrelation noises are spatially independent, we can easily derive the variance–covariance components of decorrelation noises:

$$\text{Var}(e_p - e_{r_i}) = \sigma_{e_p}^2 + \sigma_{e_{r_i}}^2 \quad (10)$$

$$\text{Cov}\left[(e_p - e_{r_i}) \cdot (e_p - e_{r_j})\right] = \sigma_{e_p}^2 \quad (11)$$

where $\sigma_{e_p}^2$ and $\sigma_{e_{r_i}}^2$ represent the variances of the two decorrelation noises at pixel p and r_i , which are estimated based on the coherences and the multi-look numbers (details can be found in Hanssen 2001). We can also find that the covariance between any of the two different MPD-based decorrelation noises is constantly equal to the decorrelation variance of the interested pixel.

2.3.3 Joint stochastic model estimation of the MPD-based displacements

After estimating the variance–covariance components of the atmospheric delays and the decorrelation noises, then we can get the joint stochastic model (i.e., variance–covariance matrix) of MPD-derived displacements, which can be written as:

$$D_{L_p} = \begin{bmatrix} \sigma_{d_p}^2(r_1) & \sigma_{d_p}^2(r_1, r_2) & \dots & \sigma_{d_p}^2(r_1, r_n) \\ \sigma_{d_p}^2(r_2, r_1) & \sigma_{d_p}^2(r_2) & \dots & \sigma_{d_p}^2(r_2, r_n) \\ \vdots & \vdots & \ddots & \vdots \\ \sigma_{d_p}^2(r_n, r_1) & \sigma_{d_p}^2(r_n, r_2) & \dots & \sigma_{d_p}^2(r_n) \end{bmatrix} \quad (12)$$

From the above analysis, we can get the variance and covariance components in \mathbf{D}_{L_p}

$$\sigma_{d_p}^2(r_i) = \gamma(h_{p,r_i}) + \sigma_{e_p}^2 + \sigma_{e_{r_i}}^2 \tag{13}$$

$$\sigma_{d_p}^2(r_i, r_j) = \frac{1}{2} [\gamma(h_{p,r_i}) + \gamma(h_{p,r_j}) - \gamma(h_{r_i,r_j})] + \sigma_{e_p}^2 \tag{14}$$

The stochastic model (\mathbf{D}_{L_p}) provides us with a wealth of quality and correlation description of the measurements that from different reference points. In Sect. 2.4, we present a minimum variance-based linear estimator to reconstruct the ground displacement by incorporating the estimated stochastic model.

2.4 Displacement reconstruction by a minimum variance-based linear estimator

Based on the basic idea of the kriging-family algorithms, which have been widely used in geostatistics and problems of optimal spatial prediction (Cressie 1990; Kaymaz 2005; Kozziel et al. 2014; Wang et al. 2015), we propose to reconstruct the displacement by using the following linear estimator:

$$\hat{d}_p = \sum_{i=1}^n [\hat{d}_p(r_i) \times \lambda_{p,i}] \tag{15}$$

where \hat{d}_p means the reconstructed displacement of d_p , and $\lambda_{p,1}, \lambda_{p,2}, \dots, \lambda_{p,n}$ represent the weights of different measurements. Considering the restriction of uniform unbiasedness ($E[\hat{d}_p(r_i)] = d_p$), we get another condition:

$$\sum_{i=1}^n \lambda_{p,i} = 1 \tag{16}$$

It is easy to find that the key point of reconstructing the displacement \hat{d}_p is to estimate the optimal weight values. We build the idea of solving the optimal weights on minimizing the theoretical variance of \hat{d}_p

$$\text{Var}\{\hat{d}_p\} = \text{Var}\left\{ \sum_{i=1}^n [\hat{d}_p(r_i) \times \lambda_{p,i}] \right\} \rightarrow \min \tag{17}$$

Based on the estimated stochastic model of L_p in Sect. 2.3, we can get

$$\text{Var}\{\hat{d}_p\} = \lambda_p \times \mathbf{D}_{L_p} \times \lambda_p^T \tag{18}$$

Jointly considering Eqs. (15)–(18), we describe our objective function as:

$$F = \lambda_p \times \mathbf{D}_{L_p} \times \lambda_p^T - 2(\lambda_p \times \mathbf{G} - 1) \tag{19}$$

where $\lambda_p = [\lambda_{p,1}, \lambda_{p,2}, \dots, \lambda_{p,n}]$ and $\mathbf{G} = [1, 1, \dots, 1]^T$ (with dimensions of $n \times 1$). By minimizing the objective function based on the method of Lagrange multipliers (Rockafellar 1993), we can obtain

$$\begin{bmatrix} \sigma_{d_p}^2(r_1) & \sigma_{d_p}^2(r_1, r_2) & \dots & \sigma_{d_p}^2(r_1, r_n) & 1 \\ \sigma_{d_p}^2(r_2, r_1) & \sigma_{d_p}^2(r_2) & \dots & \sigma_{d_p}^2(r_2, r_n) & 1 \\ \vdots & \vdots & \ddots & \vdots & \vdots \\ \sigma_{d_p}^2(r_n, r_1) & \sigma_{d_p}^2(r_n, r_2) & \dots & \sigma_{d_p}^2(r_n) & 1 \\ 1 & 1 & \dots & 1 & 0 \end{bmatrix} \begin{bmatrix} \lambda_{p,1} \\ \lambda_{p,2} \\ \vdots \\ \lambda_{p,n} \\ 0 \end{bmatrix} = \begin{bmatrix} 1 \\ 1 \\ \vdots \\ 1 \\ 1 \end{bmatrix} \tag{20}$$

It is easy to derive the optimal estimation of λ_p from Eq. (20), and the reconstructed ground displacement that has a minimum variance can also be finally obtained by Eq. (18).

The workflow of the proposed approach can be summarized as follows: (see Fig. 2): (i) we select displacement-known pixels over the whole interferogram based on the prior deforming information and the coherence; (ii) we get the MPD-derived displacements and estimate the VCM of MPDs; (iii) we reconstruct the ground displacement by using the minimum variance-based linear estimator and evaluate the uncertainties of the estimated displacement. Both Step 2 and Step 3 are processed pixel by pixel. For simplicity, we will refer to our method as MPD-InSAR (multiple phase difference-based D-InSAR approach).

3 Example using simulated data

3.1 Data simulation

As the major purpose of the proposed MPD-InSAR approach is to mitigate the turbulent atmosphere for accurately measuring the ground deformation, here our simulations of the unwrapped interferograms were only made by the addition of the atmospheric turbulence and the deformations. We consider a research region of $50 \times 50 \text{ km}^2$ with spatial resolution of about 200 m. The turbulent atmosphere was simulated based on the *Kolmogorov turbulence theory*, which predicts the one-dimensional power spectrum of the turbulence obeys a $-8/3$ and $-5/3$ power law (Hanssen 2001), three different atmospheric turbulence processes were simulated with power spectrum slopes of -1.85 , -2.25 , and -2.65 , respectively (Fig. 3a–c), and the 1D power spectrums of the simulations are presented in Fig. 3d. We consider a circular deforming region (i.e., region of interest) with zero deformations located at the central interferogram with radius of about 15 km (see the black circles in Fig. 3a–c). The deforming region would be masked for the estimation of the structure functions and the selection of the displacement-known pixels.

Fig. 2 Workflow of the MPD-InSAR approach

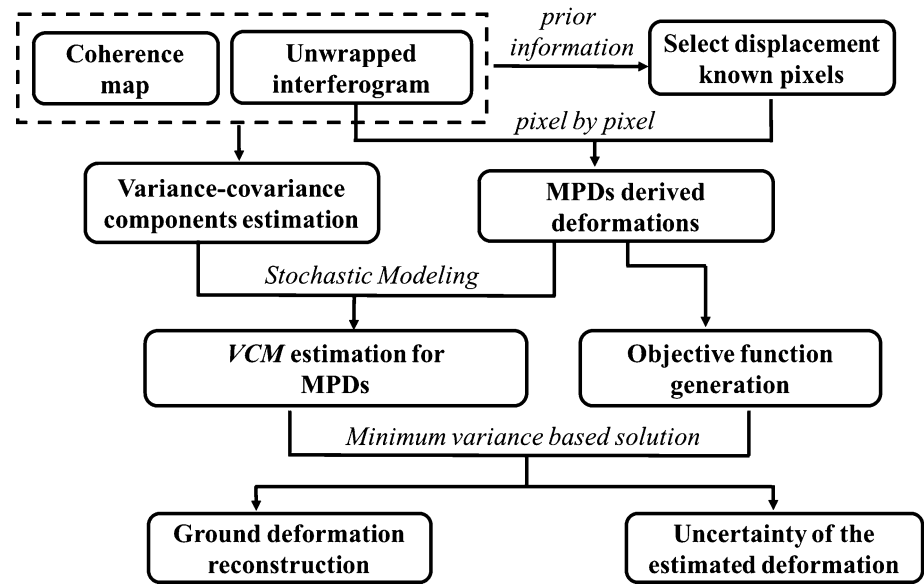
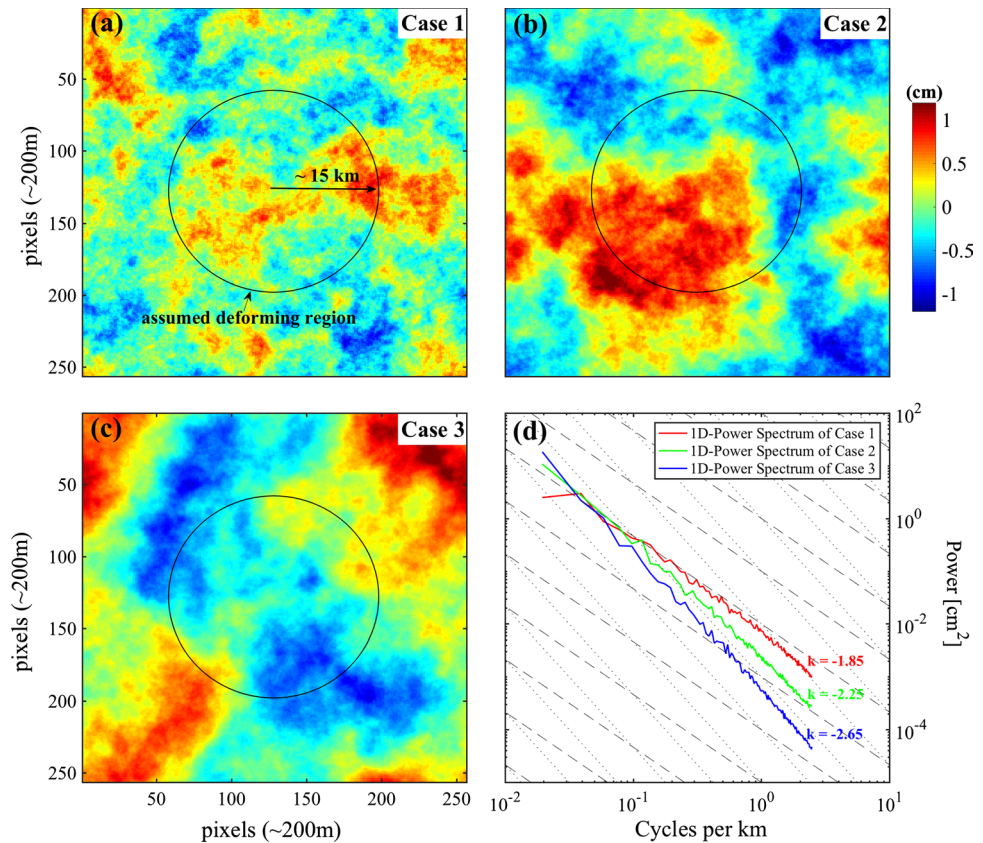


Fig. 3 a–c Simulations of the turbulent atmosphere with 1D power spectrums of -1.85 , -2.25 , and -2.65 , respectively; d the 1D power spectrums of the three turbulent fields



3.2 Deformation reconstruction

In the above simulation, we do not consider the stratified atmospheric delays, so we can skip the step of correcting this part of delays at the beginning, and we start by estimating the structure functions (i.e., variograms) using the spherical model of the three simulated turbulent fields from

5000 randomly selected points outside of the area of interest. The ranges (i.e., the maximum correlated distances) of the spherical models increase from 11 to 30.9 km (Fig. 4), consistent with the increase in the long-wavelength signals for the three turbulent random fields. We select four sets of known-displacement pixels (1, 20, 40, and 80 pixels) by random from the non-deforming (i.e., stable) region (outside of

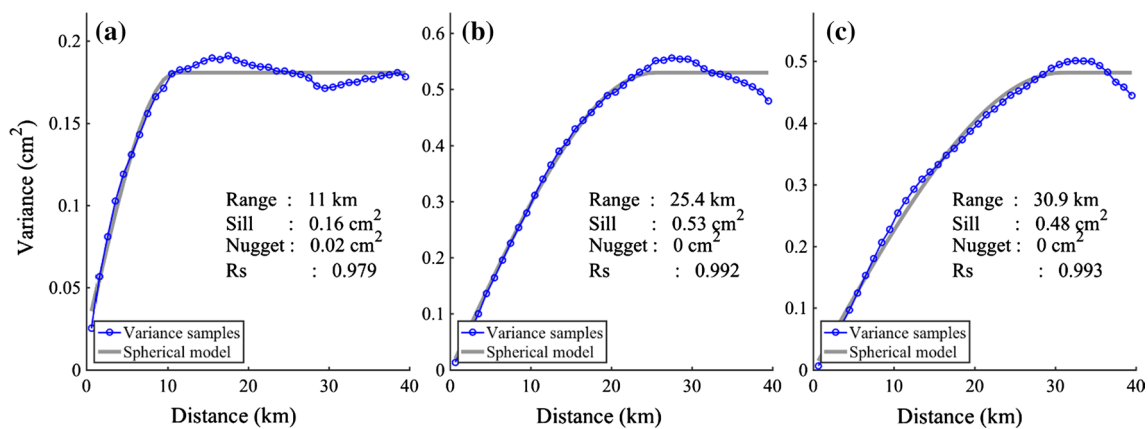


Fig. 4 Structure functions of the three turbulent fields. The blue circles are the calculated variance samples, and the gray curves are the best-fitted spherical model

the area of interest). Based on the estimated structure functions and given the locations of the selected displacement-known pixels, then we can estimate the variance–covariance matrices (VCMs) of the MPDs for each pixel of interest.

The reconstructed displacements for the three turbulence cases and three different sets of known-displacement pixels together with their histograms are presented in Fig. 5. The case of one known-displacement pixel corresponds to conventional InSAR. It should be noted that the smaller the absolute value of the reconstructed deformation is the better, as we consider the real deformations over the deforming area are zero; thus, the residual deformations also can be considered as deformation biases or errors. We find that, compared with conventional InSAR results, the MPD-InSAR-derived deformation biases are decreased significantly, and the biases become smaller and smaller with the increase in the used known-displacement pixel numbers. The accuracy and precision of a measurement are given by the mean and STD of the measurement errors, respectively. We find that for MPD-InSAR with 80 known-displacement pixels compared with conventional InSAR the means decrease by 75%, 86%, and 91% and the STD decrease by 17%, 46%, and 42% for the three cases, respectively (Table 1). This shows that (1) the accuracy and precision of MPD-InSAR are improved compared to conventional InSAR, and (2) the accuracy and precision increase with the number of known-displacement pixels. The least improvements occur in Case 1 because the mitigation of small-scale turbulence requires a higher spatial density of known-displacement pixels than the mitigation of large-scale turbulence.

A transect through the area of interest illustrates how the reconstructed displacements and their standard deviations depend on the number of displacement-known pixels (Fig. 6). The uncertainties (i.e., standard deviations) are calculated based on Eq. (18) with $\sigma = \sqrt{\text{Var}\{\hat{a}_p\}}$. It is

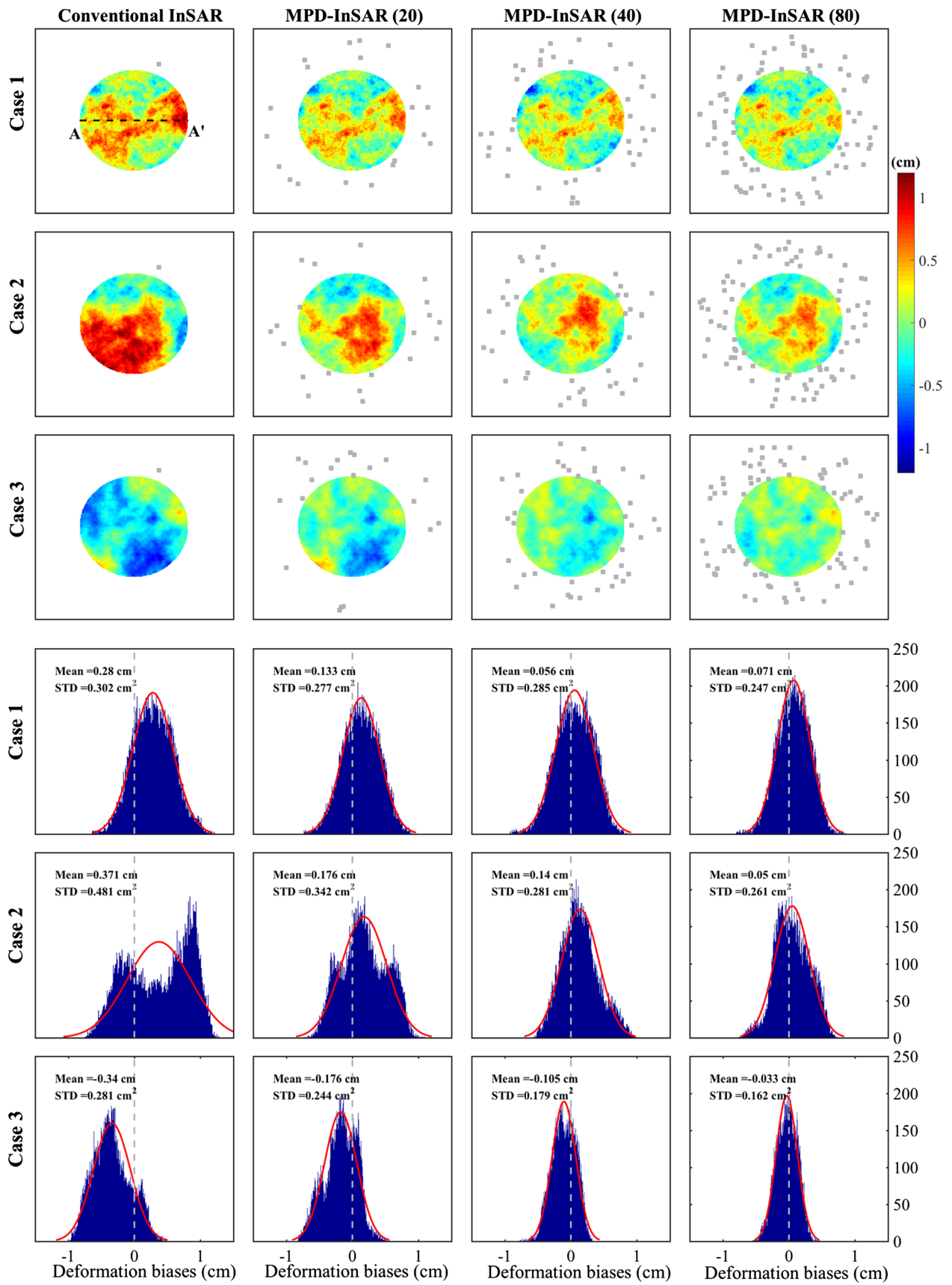
easy to find that the uncertainty of the conventional InSAR-derived displacement depends on the distance between the reference pixel and the pixel of interest, which can be calculated using the structure function directly. It can be seen that the mean absolute errors (MAEs) of the displacements (mean value of the absolute displacement biases) are smaller for MPD-InSAR than for conventional InSAR. The improvements are 52%, 50%, and 71% in the three cases, respectively.

We can see that uncertainties of the MPD-InSAR-derived deformations along the transect AA' are obviously much smaller than those of the conventional InSAR, and we can find that, in case 1, all of the deformation uncertainties of the conventional InSAR are constant and equal to about 0.42 cm; this is because of that all of the distances between the reference pixel and those pixels along the transect AA' are larger than the “range” value of the structure function. As to the MPD-InSAR-derived deformation uncertainties, it can be seen that, in general, the more the displacement-known pixels we used, the smaller the uncertainties tend to be.

4 Application to Mexico City Basin

4.1 Study area and data

Due to the extraction of groundwater in excess of natural recharge and consequent compaction of the aquifers, Mexico City has been undergoing rapid subsidence since the end of last century at rates of up to 40 cm/year in some sectors of its metropolitan area (López-Quiroz et al. 2009; Osmanoglu et al. 2011; Yan et al. 2012). Mexico City Basin can be divided into three main geotechnical zones: the Lake Zone (LZ), the Transition Zone (TZ), and the Foothills Zone (FZ) (see Fig. 3) (Yan et al. 2012).



◀**Fig. 5** Deformations and the corresponding histograms over the deforming region related to both of conventional InSAR and the MPD-InSAR (with 20, 40, and 80 displacement-known pixels, separately). The gray rectangles represent the locations of the used displacement-known pixels. The red curves in the histograms are the best-fitted Gaussian distribution functions. Results along the transect AA' in the first subfigure are presented in Fig. 6

The LZ subsoil is mainly composed of highly compressible lacustrine clays. In contrast, the subsoil over the FZ mainly corresponds to heterogeneous volcano clastic deposits and lava, and the subsidence over this region is very small and can even be ignored (around 5 mm/year in the LOS direction of ASAR in the research of Osmanoglu et al. 2011). In between, the TZ subsoil consists of gravel alluvial deposits and sand, intercalated with clay lenses and volcanic materials. The LZ is the major subsidence region of Mexico City Basin, and the FZ can be considered as a stable area. We select the displacement-known pixels from the FZ.

We obtained four Sentinel-1A SAR images and generated two 12-day interferograms (Table 2, Fig. 8) to test the proposed MPD-InSAR approach. The interferograms are processed using the ISCE (InSAR Scientific Computing Environment) software (Rosen et al. 2012). Precise Orbit Ephemerides (POE) data are used for the orbital parameters estimation, and the topography and flat earth-related phases are removed based on the 30-m SRTM DEM, and the interferometric phases are unwrapped by using the minimum cost flow method.

4.2 Selection of displacement-known pixels

We selected the displacement-known pixels (non-deforming pixels) from foothills zone with coherence large than 0.95 and elevations under 2400 m. Coherence maps showing the areas of potential displacement-known pixels and the corresponding DEM (with elevations smaller than 2400 m) are illustrated as Fig. 9a–c. Because the elevations of the candidates of the displacement-known pixels are very close to those of the to-be-estimated pixels (i.e., deforming pixels over the area of interest), the possible stratified atmospheric delays in the phase difference (between the reference and to-be-estimated pixel) can be ignored and need not to be corrected explicitly. In addition, considering the spatial correlation of the atmospheric delays, we select the pixels as close to the deforming area as possible. We selected 120 displacement-known pixels (gray rectangles in Fig. 9d, f) for the deformation reconstruction, and the coherences and elevations of the selected pixels are shown as Fig. 9e, g for the two interferograms, respectively.

4.3 Stochastic modeling for multiple phase differences

The spatial variance samples of the turbulent atmospheric delays are estimated by using the interferometric phases over the Foothills Zone (i.e., non-deforming zone) with coherence larger than 0.8 and elevations smaller than 2400 m, so that the effects of both the decorrelation noises and the possible stratified atmosphere on the estimation of the structure function model of the turbulent atmospheric delays would be very limited. The estimated variance samples and the best-fitted spherical models are shown in Fig. 10. It can be seen that the “Ranges” of the two structure functions are very similar (23.4 and 23.3 km), and the maximum variances (sum of the “Sill” and the “Nugget”) of the turbulent atmospheric delays could be up to 0.87 and 0.96 cm², respectively, when the distance between the two points is longer than the “Ranges”. We can see that the turbulence-caused variances of the two interferograms can be up to close 1 cm, and this is even larger than the possible maximum displacements (~40 cm per year) over the research region during 12 days. Therefore, it is certainly difficult to extract the real displacements over the region of interest from the original interferograms (Fig. 5a, b).

Based on the structure function models and the spatial locations of the displacement-known pixels, we can estimate the VCM (with dimensions of 120 × 120) of the MPDs pixel by pixel. Taking a pixel p_0 (black triangle in the bottom left plot of Fig. 11) as an example, we present the two interferogram-based VCMs of the MPDs as Fig. 11a (ascending) and b (descending). It should be noted that the VCMs of the MPDs are varied pixel by pixel, due to that the spatial geometry between the pixel of interest and the displacement-known pixels is changed for different interested pixels, so both the variances and the covariances of the MPDs would change for different pixels.

4.4 Ground displacement reconstruction

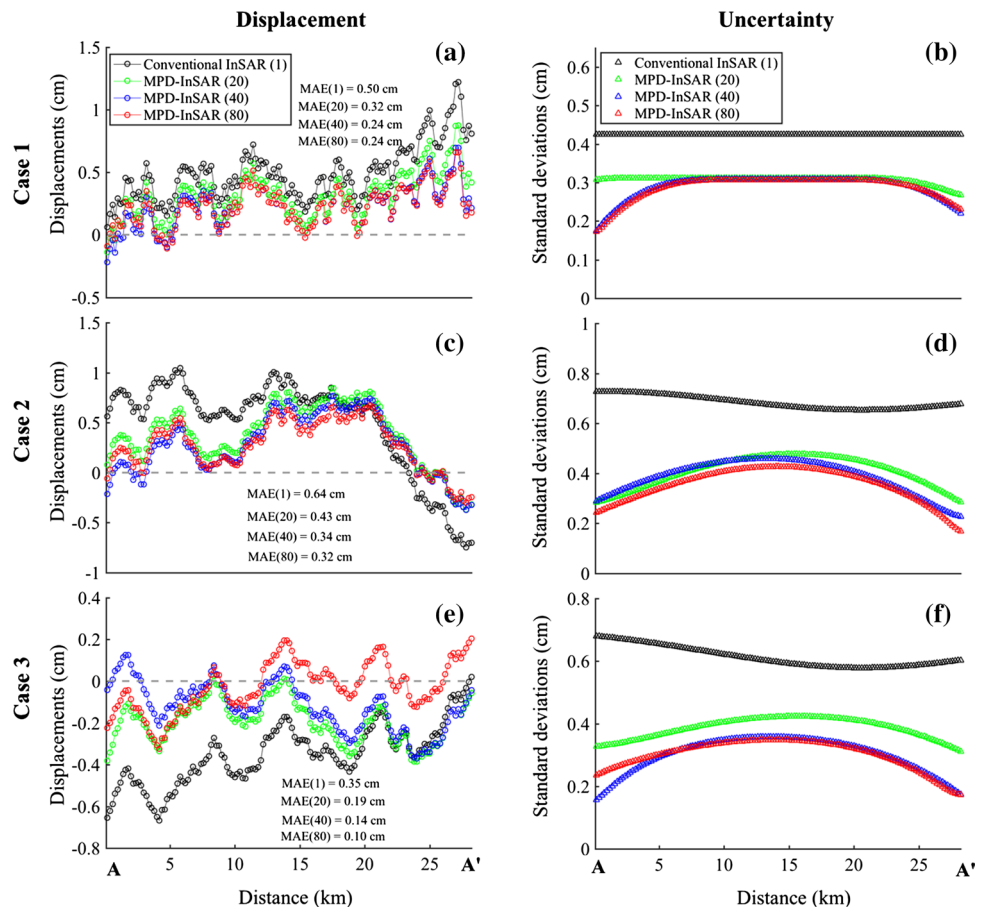
Ground displacements over the region of interest are reconstructed by using the MPD-InSAR approach (see Fig. 12). We focus on evaluating the precision of the MPD-InSAR-derived displacements. In the northwestern part of the ascending interferogram over Mexico City region, the effects of the turbulent atmosphere are very significant (Fig. 12a), and in the southeastern part of the whole descending interferogram those turbulent delays have almost dominated all of the possible displacements (Fig. 12b). Thus, it is difficult to extract the possible ground displacements, which should be mainly occurred over the Lake Zone (inside the red line), from the conventional InSAR interferograms. In contrast, those turbulent atmospheres, occurred in conventional InSAR-based results, are corrected efficiently for the

Table 1 Summary of the mean values (unit: cm) and the standard deviations (unit: cm) of the deformation biases

	Case 1 ($k = -1.85$)				Case 2 ($k = -2.25$)				Case 3 ($k = -2.65$)			
	Mean	Imp. (%)	STD	Imp. (%)	Mean	Imp. (%)	STD	Imp. (%)	Mean	Imp. (%)	STD	Imp. (%)
Conventional InSAR (1)	0.28	–	0.30	–	0.37	–	0.48	–	–0.34	–	0.28	–
MPD-InSAR (20)	0.13	53	0.28	7	0.18	51	0.34	29	–0.18	47	0.24	14
MPD-InSAR (40)	0.05	82	0.29	3	0.14	62	0.28	42	–0.10	70	0.18	35
MPD-InSAR (80)	0.07	75	0.25	17	0.05	86	0.26	46	–0.03	91	0.16	42

The percentage improvements (Imp.) of the MPD-InSAR results are with respect to conventional InSAR results

Fig. 6 Experimental results along transect AA'. The first column is related to the displacement, and the second column is related to the uncertainty (i.e., standard deviation) of the corresponding deformations for the three cases, respectively



MPD-InSAR-derived results. Two significant deforming regions, one from southwestern region of Nabor Carrillo and another from near Zona de Reserva Ecologica region, can be seen from Fig. 12c, d. The standard deviation (STD) maps of the reconstructed displacements calculated based on Eq. (18) are shown in Fig. 13. It can be seen that the original D-InSAR-based STDs are strongly correlated with the distances between the pixels of interest and selected reference pixel (gray rectangle at the northeastern part), and the STDs can be up to when the distance is close or over the “range” values (23.3 and 23.4 km for the two interferograms). Compared with the original D-InSAR results, MPD-InSAR-based STDs (Fig. 13c, d) are decreased significantly (less than

0.5 cm) for both the ascending and descending interferograms. This suggests that the effects of the turbulent atmosphere are corrected efficiently in the two interferograms.

4.5 Results evaluation

Considering that the maximum displacements over Mexico City is around 40 cm/year, we can safely consider that the real displacements during 12 days should be less than 1.5 cm. Besides, we can also get that the subsidence-related LOS displacements should be negative values (move away from the satellite) in our experiments. Thus, those displacements not between -1.5 and 0 cm can be considered as

Fig. 7 Shaded SRTM (shuttle radar topography mission) elevation relief over the Mexico City region. The light blue and red lines represent the Lake Zone (highly compressible) and Transition Zone (TZ), respectively. The area outside the red line is the Foothills Zone (stable area)

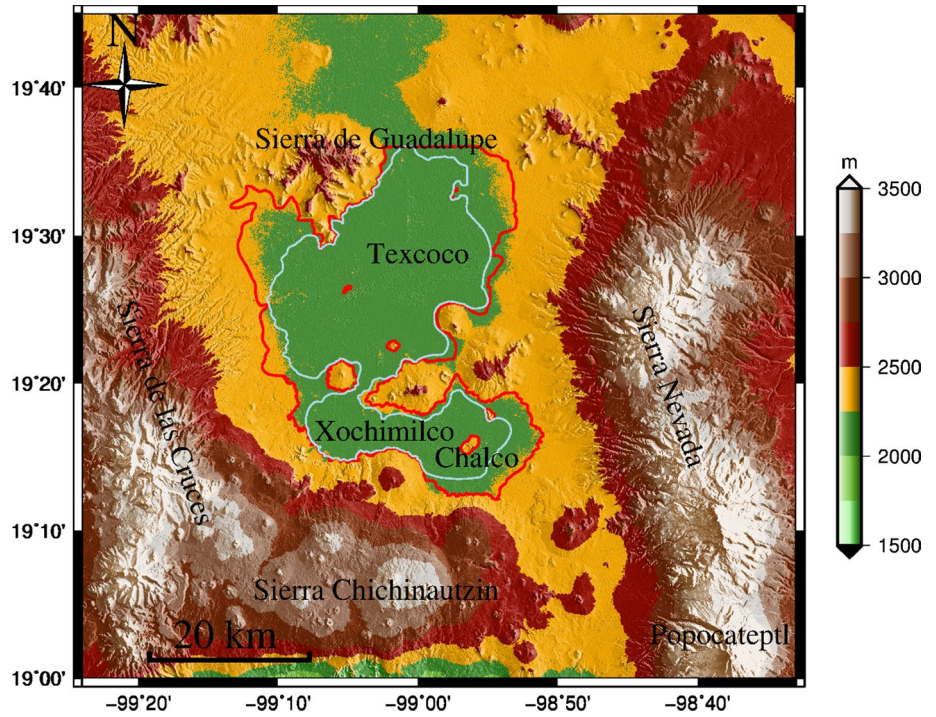
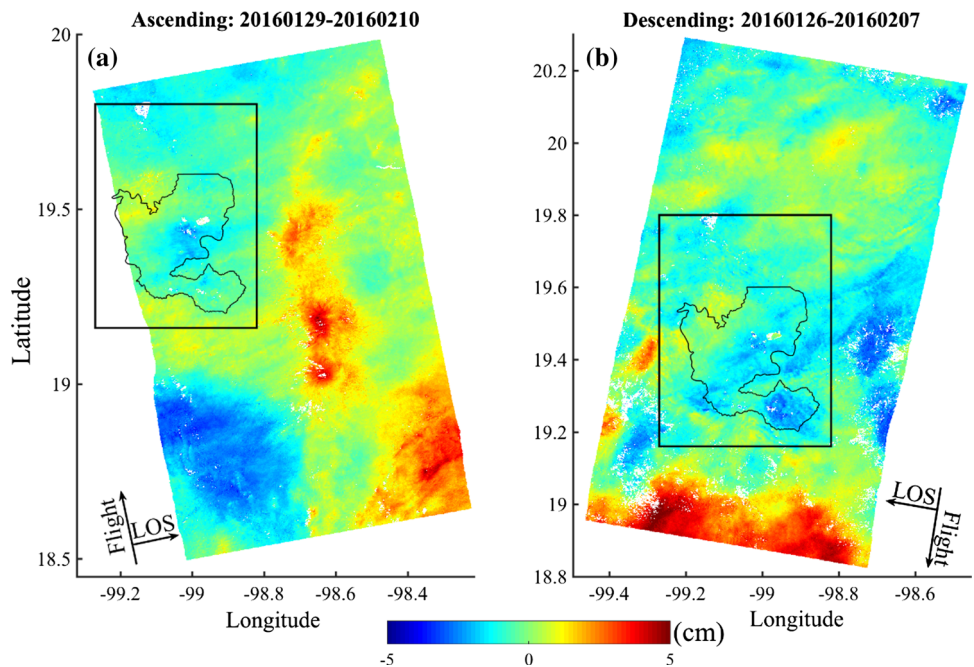


Table 2 Details of the used Sentinel-1A images

Date	Platform	Orbit	Track	Swath
January 29, 2016	Sentinel-1A	Ascending	5	1
February 10, 2016	Sentinel-1A	Ascending	5	1
January 26, 2016	Sentinel-1A	Descending	143	3
February 7, 2016	Sentinel-1A	Descending	143	3

false deformation signals. Based on this, we calculated the percentages of the false displacement signals over the Laker Zone, which are shown in Table 3. We can see that the percentages of the conventional InSAR-based false deformation signals over the Laker Zone reach to 39.4% and 45.1% for the ascending and descending interferograms, while those of the MPD-InSAR-derived false signals are decreased

Fig. 8 Geocoded unwrapped differential interferograms over Mexico City with a spatial resolution of 30 m × 30 m: **a** ascending interferogram (20160129-20160210); **b** descending interferogram (20160126-20160207). The black rectangle accounts for further research region that includes Mexico City region, and the thin black line represents the outside edge of the Foothills Zone (see Fig. 7)



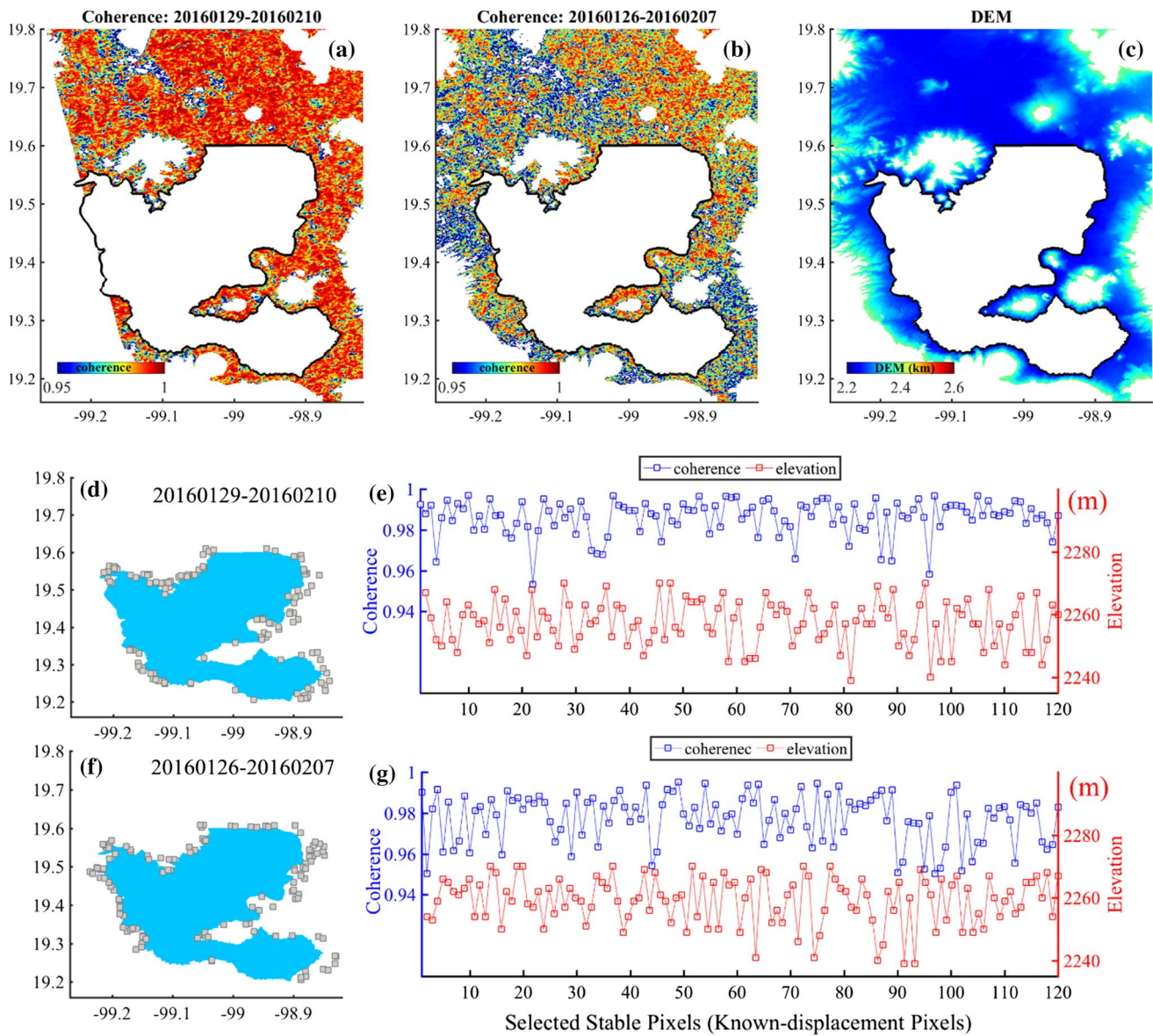


Fig. 9 a, b Coherence maps that related to the potential areas of selecting the displacement-known pixels, c corresponding DEM maps with elevations smaller than 2400 m; d, f locations of the selected

pixels; e, g the corresponding coherences and elevations of the selected displacement-known pixels

to 22.8% (improved by 42.1%) and 18.5% (improved by 71.5%), respectively.

The displacements along two profiles are presented in Fig. 14, where AA' profile across the major northern part of Mexico City and BB' transect the southern part (see the left plot of Fig. 14). The red circles represent the reconstructed displacements from the MPD-InSAR approach, and the gray error bar means the STDs (plus and minus) of the MPD-InSAR-based displacements. The blue circles represent the original D-InSAR-based displacements. We can find that the original D-InSAR-based displacements are seriously biased; for example, the displacements

close to the Transition Zone (near the breaking points) in Fig. 14a, b, d can reach to 2 cm, which should be close to 0, and the maximum subsidence in Fig. 14b, d (close to 3 cm) is significantly overestimated. As to the MPD-InSAR-derived displacements (red circles), we can see that those biases (occurred in the original D-InSAR results) are well mitigated, and the maximum LOS displacements along AA' profile (occurred close to Cola de Pato region) reach to around 1.5 cm (with an uncertainty of around 5 mm) during 12 days in both ascending and descending images, and the maximum displacements along BB' profile (occurred close to the northwestern area of Lake Chalco)

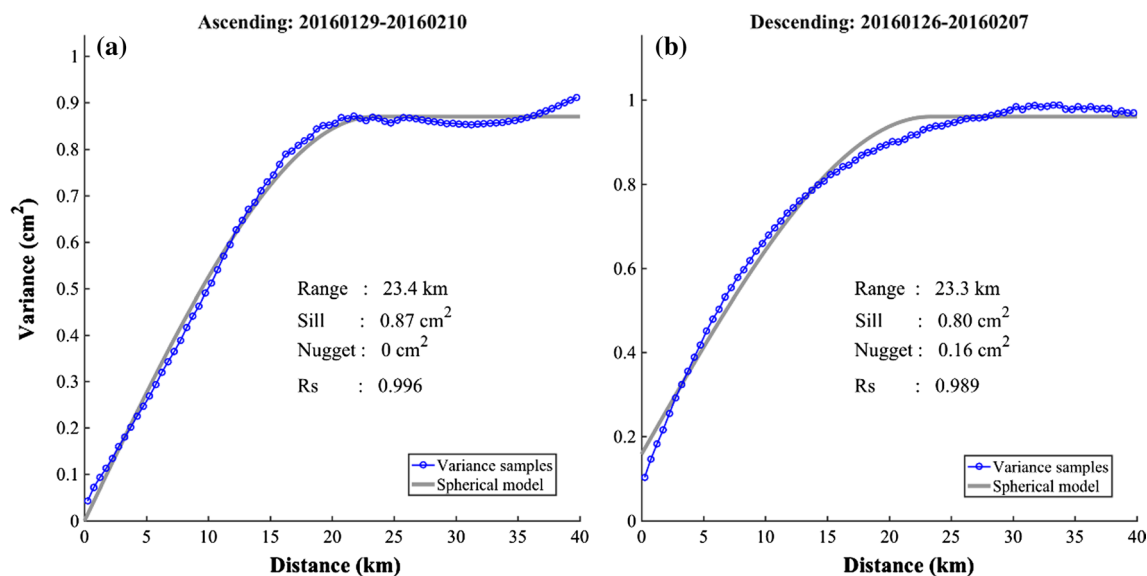


Fig. 10 Structure function of the turbulent atmospheric delays in the two interferograms: **a, b** the structure function of the ascending and descending interferograms. The blue circles represent the variance samples and the gray line denotes the best-fitted spherical model

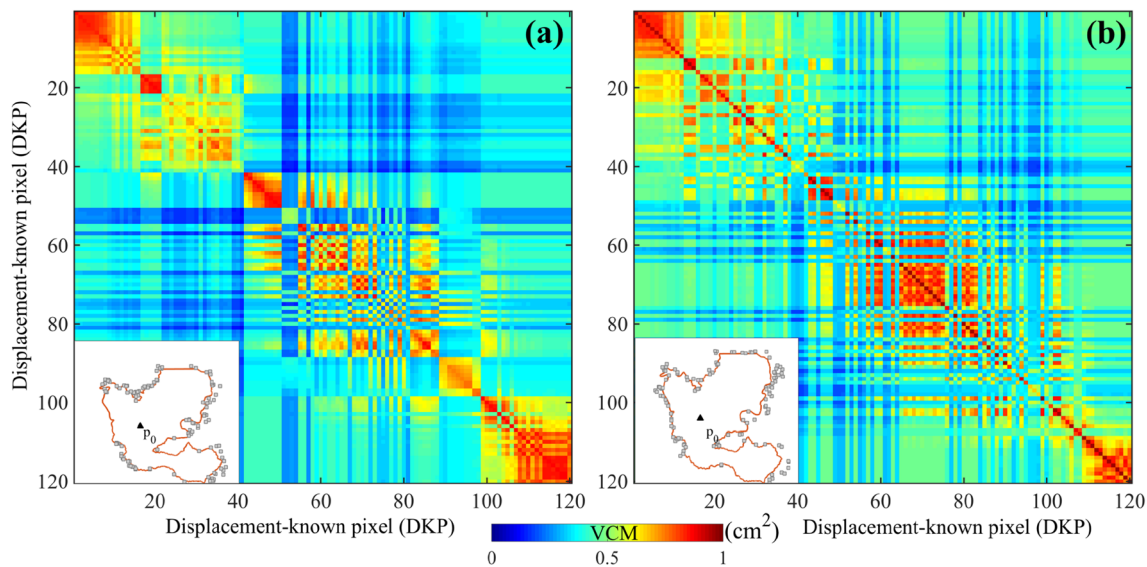


Fig. 11 Variance-covariance matrixes of the MPD-InSAR measurements at pixel p_0 (see the bottom left plot) for the two interferograms: **a, b** the ascending and descending interferogram-based VCMs, respectively

reaches to around 1.6 cm (with an uncertainty of around 4 mm) in the two interferograms.

We cross-validate the performance of the MPD-InSAR approach by evaluating the absolute differences between the subsidence derived from the ascending and descending interferograms. Considering that the radar LOS displacements over Mexico City region are mainly caused by ground subsidence (Osmanoğlu et al. 2011; Yan et al. 2012), we can convert them to vertical displacements using $d_{up,p} = d_{los,p} / \cos(\theta_{inc,p})$, that $d_{up,p}$ is the vertical

displacement at pixel p , $d_{los,p}$ accounts for the InSAR-derived LOS displacement and $\theta_{inc,p}$ denotes the radar incidence angle. Because the time periods of the two interferograms are very close (20160129–20160210, 20160126–20160207), the subsidence during the two periods should be very similar. Based on this fact, histograms of the absolute differences show that 9% of the MPD-InSAR absolute differences are larger than 10 mm compared to over 25% for conventional InSAR (see Fig. 15), and the mean of the absolute differences is 4.5 mm for MPD-InSAR compared to 8.5 mm for

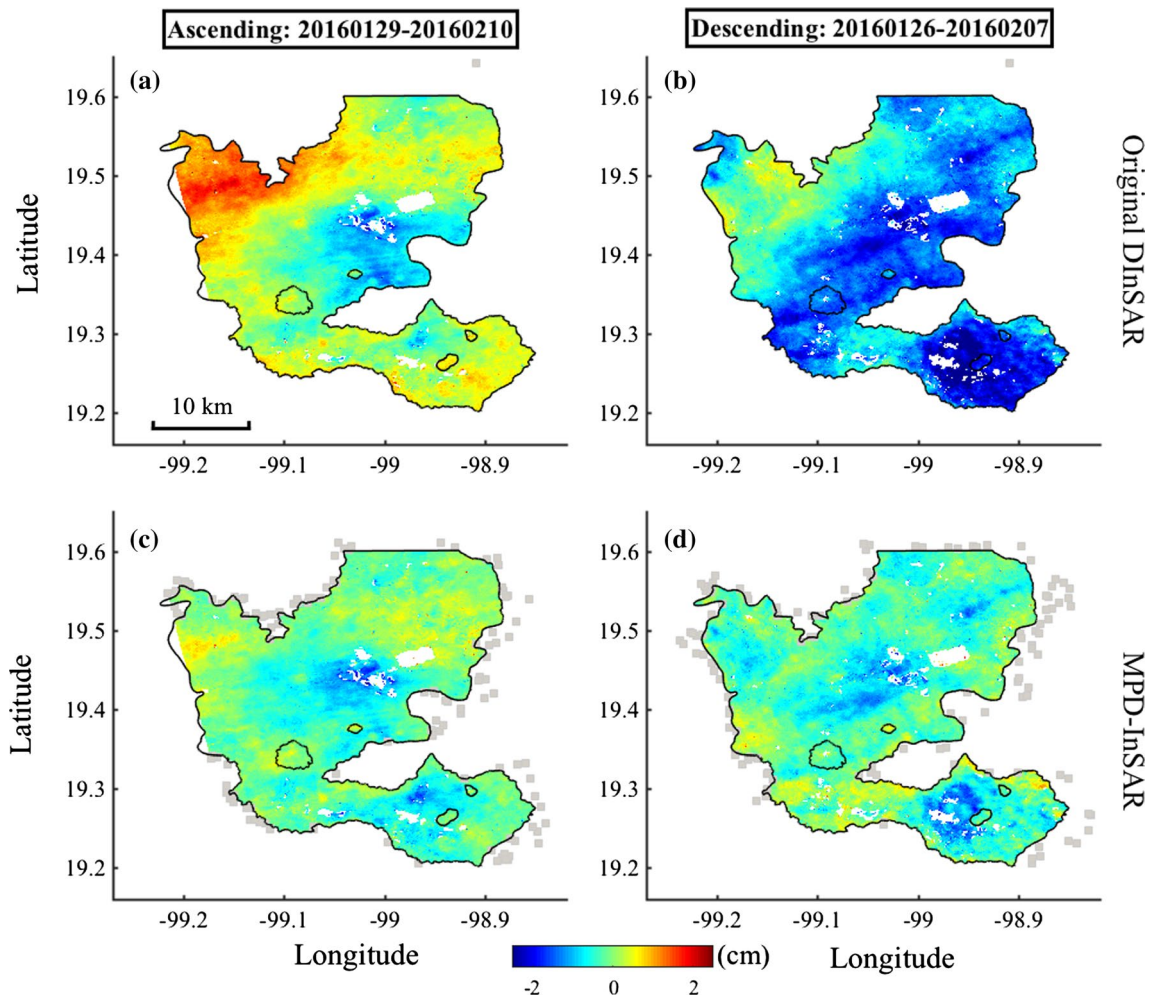


Fig. 12 Comparisons between D-InSAR- and MPD-InSAR-based displacements: **a, b** original D-InSAR-based displacements; **c, d** the MPD-InSAR-based results by using 120 reference points. The gray rectangles mean the locations of the selected displacement-known

pixels, and the black line responds to the edge of the Foothills Zone. Positive values mean move toward the satellite and negative values respond to move away from the satellite

conventional InSAR. The smaller differences in subsidence between ascending and descending interferograms for MPD-InSAR compared to conventional InSAR implies that the MPD-InSAR performs well for the mitigation of the turbulent atmosphere.

5 Discussion

5.1 Effect of the number of the displacement-known pixels

It is easy to find that the amount of the used displacement-known pixels plays a key role in the performance of MPD-InSAR approach. Let us take the descending Sentinel-1A interferogram (20160126–20160207) as an example to do a further discussion.

We test four different amounts (10, 20, 40 and 120) of the used displacement-known pixels, and we control the effects of the spatial distribution (this will be discussed separately) of the selected pixels by selecting the known pixels randomly from the previously used known pixels (e.g., we select the 40 known pixels randomly from the afore used 120 known pixels, and then, we select 20 known pixels randomly from the afore used 40 known pixels). STD maps of the MPD-InSAR-derived displacements are shown as Fig. 16a–d for the four situations ($N=10, 20, 40$ and 120), respectively, and the STDs along profile AA' are illustrated in Fig. 16e. It can be seen that with the increase in the known-pixels number, the STDs of the reconstructed displacements are becoming smaller and smaller. Ten known-pixel-based STDs can be up to 8 mm (like southeastern part of the research region), and the 120 known-pixel-based STDs are all decreased to around 5 mm. In order to evaluate this effect quantitatively,

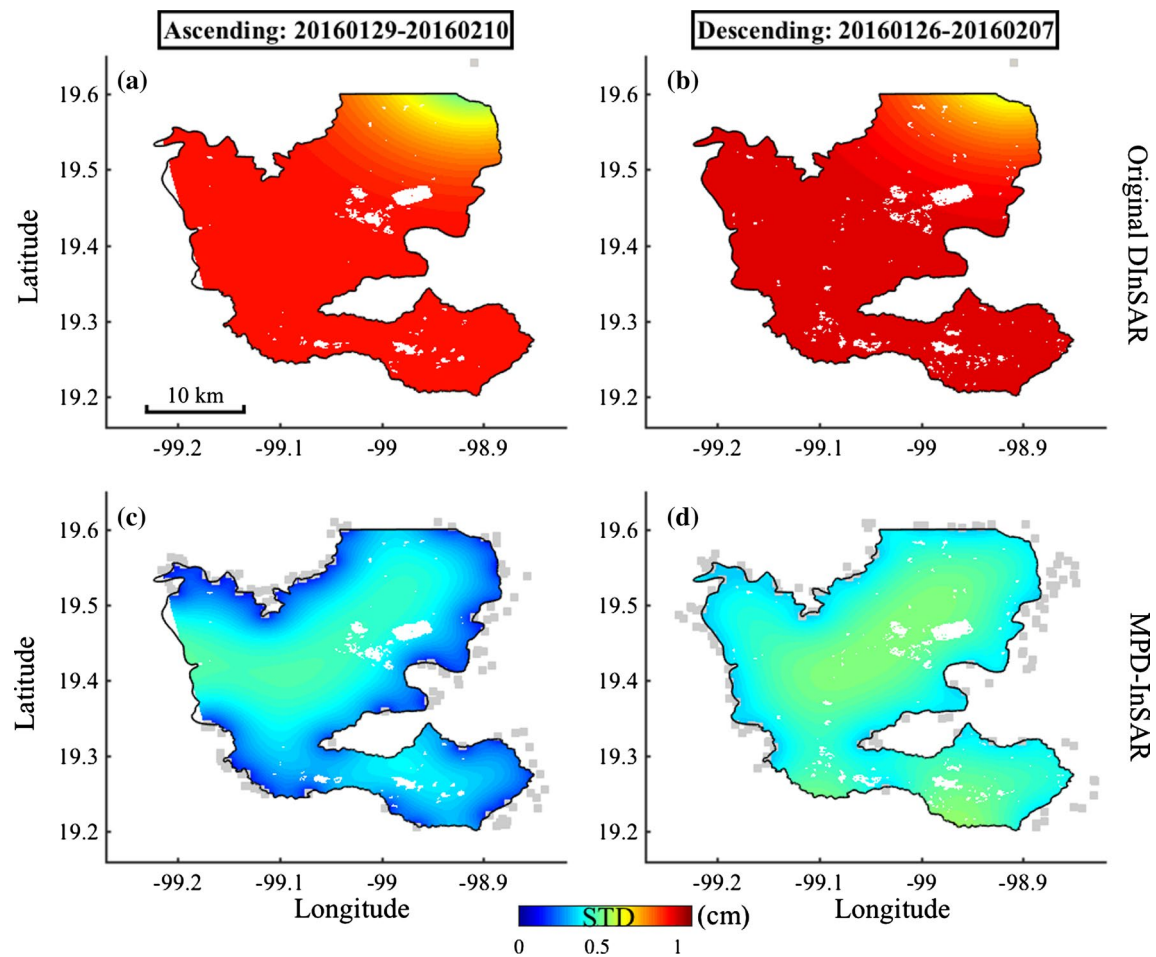


Fig. 13 Standard deviations (STD) of the displacements: **a, b** the STD maps of the original D-InSAR-based LOS displacements (estimated based on the isotropic spherical model of the turbulent atmosphere); **c, d** the STD maps of the MPD-InSAR-based LOS displacements

Table 3 Summary of the false displacement signals in the ascending and the descending interferograms

Methods/data	Ifg1/ascending		Ifg2/descending	
	False signals	Ratio (%)	False signals	Ratio (%)
Conventional InSAR	280,306	39.4	450,906	45.1
MPD-InSAR	162,331	22.8	128,349	18.5

we test the improvement (i.e., decreasing) of the STDs with the increase in the known-pixels number (increase from 5 to 120 with a step size of 5) at three different points on AA' profile (p_1 , p_2 and p_3 in Fig. 16a), and we repeat 300 times by selecting the known pixels randomly around the interested region for each known-pixels number sample to get an average STD. Relationship between STDs and the used known-pixels number is presented in Fig. 17. We can find that, compared with 5 known-pixel-based STDs, the 120 known-pixel-derived STDs are improved by 27% (from 6.5

to 4.7 mm), 23% (from 7 to 5.4 mm), and 31% (from 6.7 to 4.6 mm) for the three points, respectively. The STDs' decreasing ratios are shown in Fig. 17b, and we can see that the change ratios of the STDs are decreased rapidly with the increase in the known-pixels number, the decreasing ratios for 10 known pixels can be up to around 0.01 cm/point, this means when we use one more reference point, the STD would decrease 0.01 cm. When the known-pixels number reaches to 60, the ratio is decreased to around 0.001 cm/point. This shows that the results improve with the number of displacement-known pixels, but that the improvement tends to stop with further increased number of pixels.

5.2 Effects of spatial distribution of the used displacement-known pixels

As analyzed before, the spatial distribution (i.e., spatial geometry) of the displacement-known pixels would also affect the performance of MPD-InSAR. In other words, even we use the same number of the known pixels, the

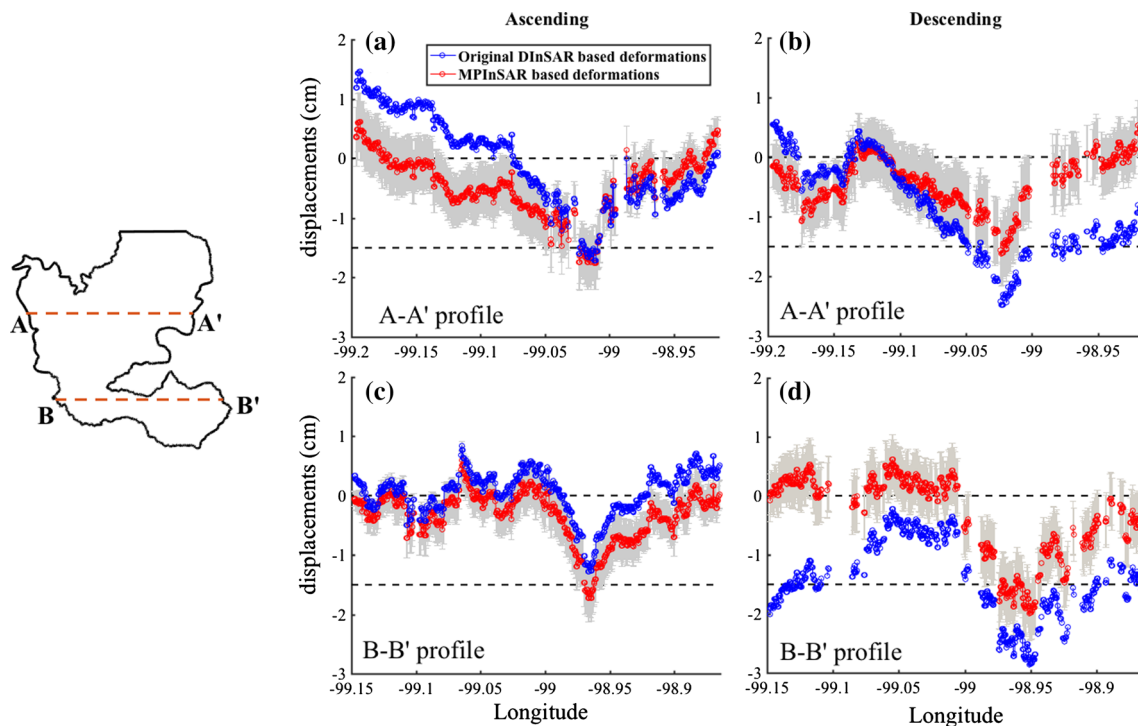


Fig. 14 Displacements along the AA' and BB' profiles: **a, b** the AA' profile-related results correspond to the ascending and descending interferograms, respectively; **c, d** the BB' profile-related results. The

gray error bar represents the STDs (plus and minus) of the MPD-InSAR-based displacements

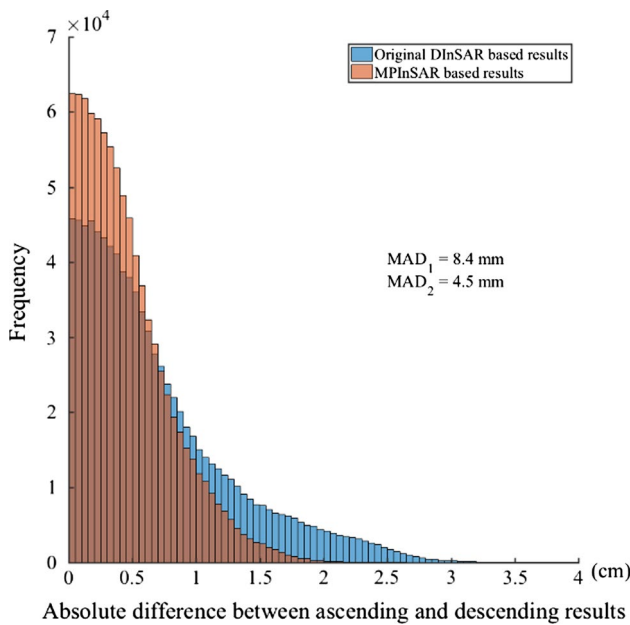


Fig. 15 Absolute differences between ascending and descending interferogram-based ground subsidence

MPD-InSAR-derived displacements and their precision (i.e., standard deviations) would be different if the spatial distributions of the known pixels are different.

Let us consider a circle-interested area with a same turbulent structure function of the ascending interferogram over Mexico City, and we test the theoretical standard deviations of the MPD-InSAR-based ground displacements under three situations: (1) 10 known pixels distributed uniformly around the deforming region with a same radius of 20 km; (2) 10 known pixels distributed around the half part of the deforming region; (3) the known pixels distributed around only one-sixth part of the deforming circle. Results are presented in Fig. 18, and the black rectangles represent the selected displacement-known pixels. It is easy to find that the spatial geometry of the selected known pixels has a big influence on the final results, and the first situation-based results are obviously better than the other two situations as a whole, especially in the northern part of the interested region. The three related variance-covariance matrixes of pixel p_0 are presented as Fig. 19. Because the distances between the known pixels and the pixel of interest are all equal to 20 km, variances (diagonal elements) of MPD-derived displacements are all equal to 1.76 cm^2 . While it can be seen that there are big differences among the covariances (non-diagonal elements) and covariances of the third situation (known pixels distributed around the one-sixth of the deforming circle are obviously larger than that of the other two situations), this implies that the correlations among the known pixels in Fig. 18c are much stronger

Fig. 16 Standard deviation of MPD-InSAR-derived displacements by using different numbers of the selected known pixels: **a-d** the MPD-InSAR-based STD maps by using 10, 20, 40 and 120 known pixels (the gray rectangles account for the locations of the used reference point); **e** the MPD-InSAR-based STDs along AA' profile, and the black, blue, green and red curves correspond to 10, 20, 40 and 120 displacement-known pixels, respectively

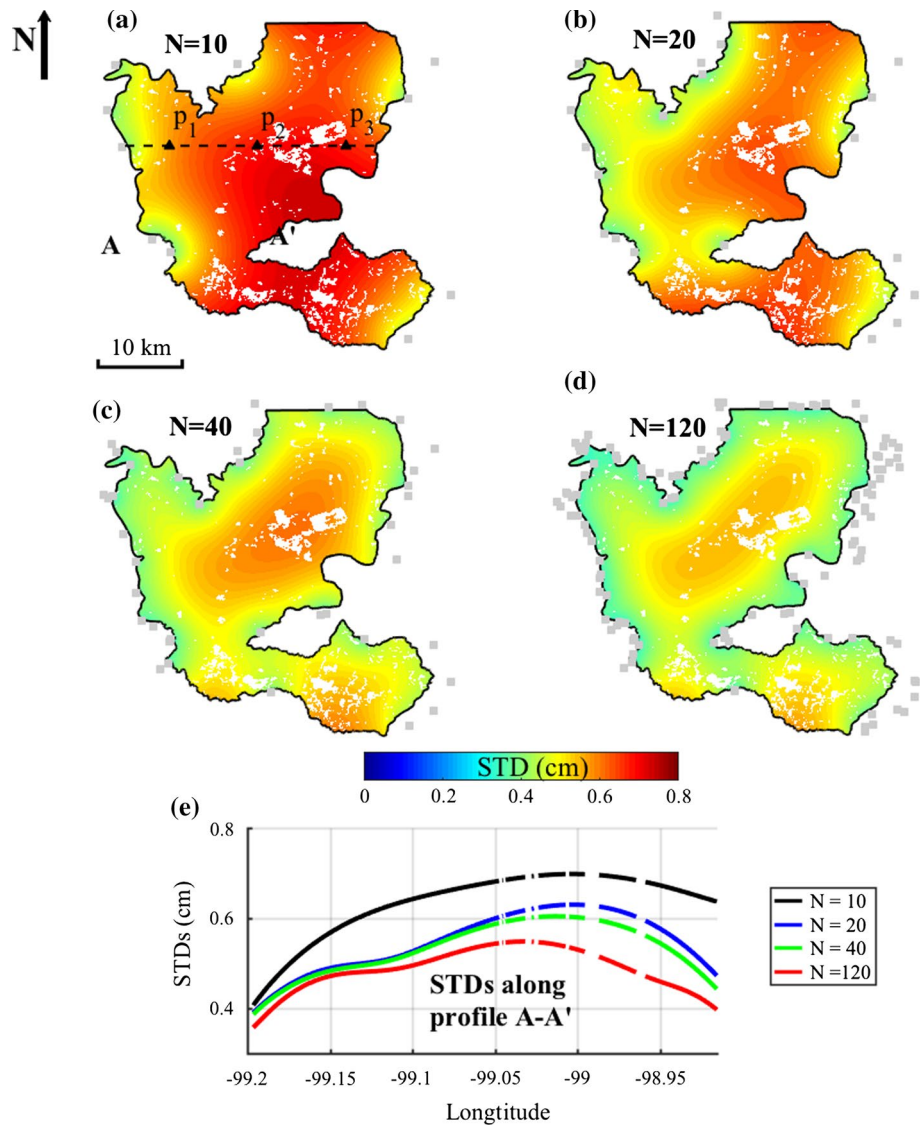
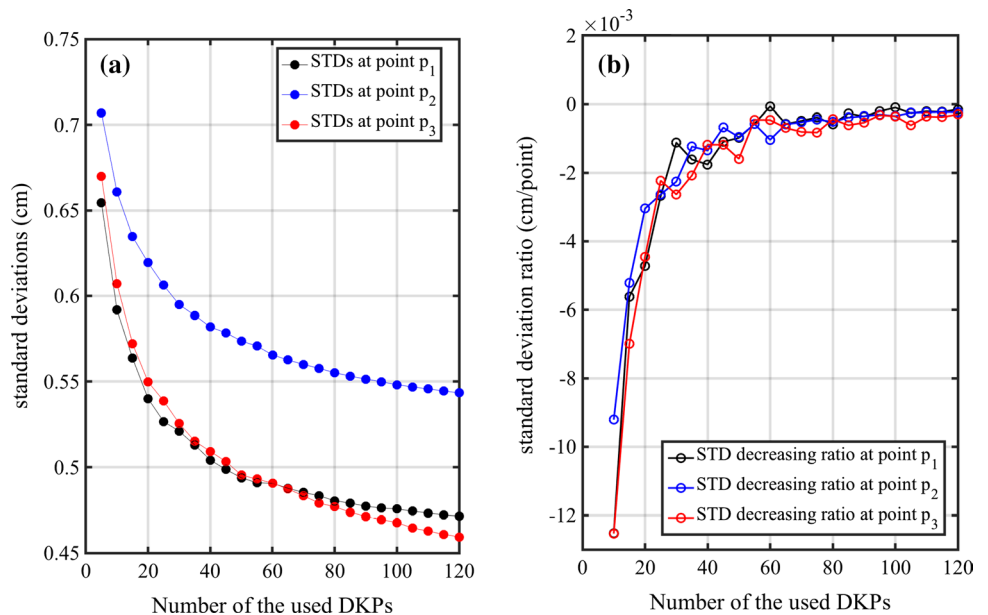


Fig. 17 Relationship between known-pixels amount and STDs: **a** STD changing trends for the three different points; **b** the STD decreasing ratios with the increase in the known-pixels amount



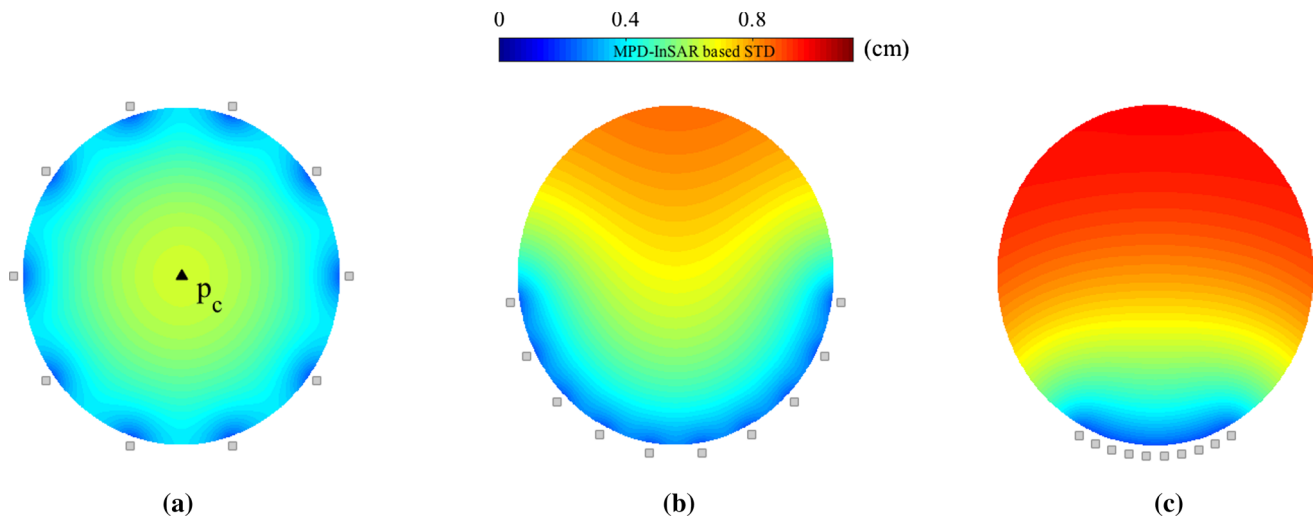


Fig. 18 Three spatial distribution situation-based standard deviations: **a** 10 known pixels distributed uniformly around the deforming region with a same radius of 20 km; **b** 10 known pixels distributed around the half part of the deforming region; **c** the known pixels distributed around only one-sixth part of the deforming circle

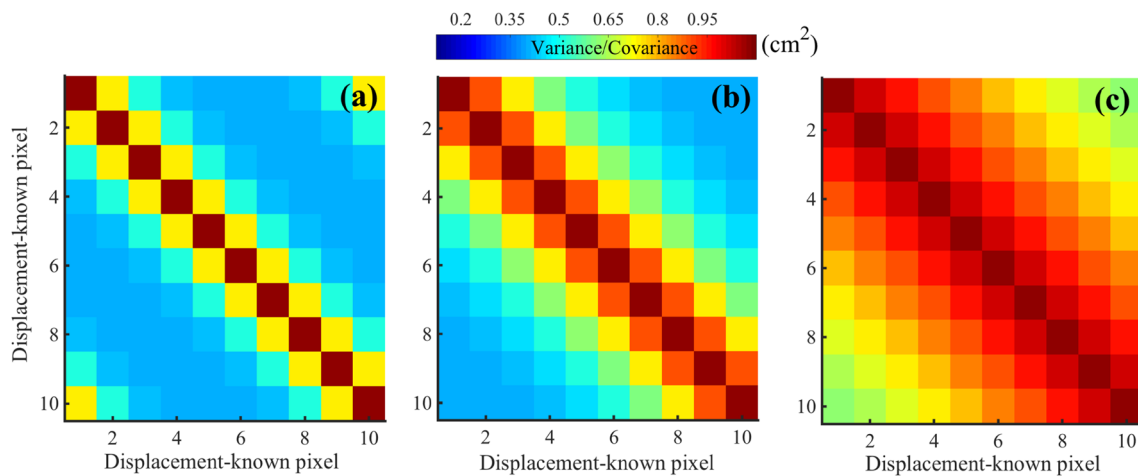


Fig. 19 VCMs of MPD-InSAR measurements at pixel p_0 (central point of the interested region): **a** selected known pixels distributed uniformly around deforming region; **b** selected known pixels distributed around half circle of the interested region; **c** selected known pixels distributed only around the one-sixth of the deforming circle

than the other two situations. This suggests that correlation between the known pixels plays a negative influence on the performance of the MPD-InSAR approach, and we should select the known pixels as uniformly distributed as possible around the interested regions.

5.3 Effects of the displacement errors of the selected displacement-known pixels

The displacements errors of the known pixels would obviously affect the MPD-InSAR-derived displacements. However, variances (or uncertainties) of the used prior displacements of

the known pixels are usually unknown and difficult to model; we do not consider their stochastic model in Sect. 2.4. Here we assume that the variances of the prior displacements are known, and further consider that the prior displacement errors are independent; then, the VCM model of MPD-InSAR measurements (Eq. 12) can be transformed into:

$$D'_{L_p} = D_{L_p} + \begin{bmatrix} \sigma_{r_1}^2 & & & \\ & \sigma_{r_2}^2 & & \\ & & \ddots & \\ & & & \sigma_{r_n}^2 \end{bmatrix} \quad (21)$$

where D'_{L_p} is the new VCM model that is meant to take the prior displacement errors into consideration, and D_{L_p} accounts for the original VCM model (see Fig. 16), $\sigma_{d_r}^2$ ($i = 1, 2, \dots, n$) represents the variance of the prior displacement error of the i th known pixel. Theoretical variance of the MPD-InSAR-derived displacements (see Eq. 18) can be re-defined as:

$$\text{Var}\{\hat{d}_p\} = \lambda_p \times D'_{L_p} \times \lambda_p^T \tag{22}$$

In order to test the effect of the prior displacement errors on the MPD-InSAR results, we take the descending interferogram over Mexico City region (20160126–20160207) as an example, and we choose the point p_1 (see Fig. 16a) to do a further analysis. Three situations are considered: (1) 1/2 of the known pixels have prior displacement errors; (2) 3/4 of the known pixels have errors; (3) all of the selected known pixels with displacements errors, and we assume that the displacements errors have the same uncertainties and test three levels: (1) $\sigma_{d_r}^2 = 0.1 \text{ cm}^2$; (2) $\sigma_{d_r}^2 = 0.3 \text{ cm}^2$; (3) $\sigma_{d_r}^2 = 0.5 \text{ cm}^2$. This means the uncertainties (i.e., standard deviation) of the displacement errors can be up to 3, 5, and 7 mm, respectively. For each case ($3 \times 3 = 9$), we repeat 300 times to get an average value by selecting the known pixels randomly and also choosing those biased displacement-known pixels randomly. We estimate the weights vector (Eq. 20) by using the original VCM (that does not consider the prior displacement error), and we calculate the standard deviation of the reconstructed displacement based on the new VCM by using Eq. (22). Standard deviations of the

MPD-InSAR-derived displacements that consider the prior displacement errors are presented in Fig. 16. We can find that, if the used prior displacements are biased and we do not consider those biases in our stochastic model, the evaluated uncertainties of the reconstructed displacements would be underestimated. It can be seen that, when uncertainties of the prior displacement errors are around 3 mm ($\sigma_{d_r}^2 = 0.1 \text{ cm}^2$), effects of prior displacement errors are very limited and four kinds of STDs are very close (see Fig. 20a). With the rise of the uncertainties of the prior displacements, uncertainties of the MPD-InSAR-derived displacements also tend to be increased. In addition, the more known pixels have errors, the worse results tend to be. We also can find that, even all of the known pixels have prior displacement errors (i.e., biases), the more the known pixels we used, the better the results we can get. Like that in Fig. 20c, even all the known pixels have an uncertainty of 7 mm ($\sigma_{d_r}^2 = 0.5 \text{ cm}^2$), when we use up to 120 reference points, STDs of the MPD-InSAR-derived displacements also can be decreased to below 5.5 mm (that of the original conventional InSAR-derived result is around 1 cm, see Fig. 13b).

In practice, it is really not possible to make sure all of the used prior displacements (assume to be zero for selected “stable” points or obtain from external displacement dataset) have no biases, what we can do is to control all of the selected displacement-known pixels as stable (un-deformed) as possible. From our experiments, we can conclude that, even all of the used known pixels have prior displacement errors (even up to 7 mm), the MPD-InSAR approach still performs well for reconstructing the true ground displacements.

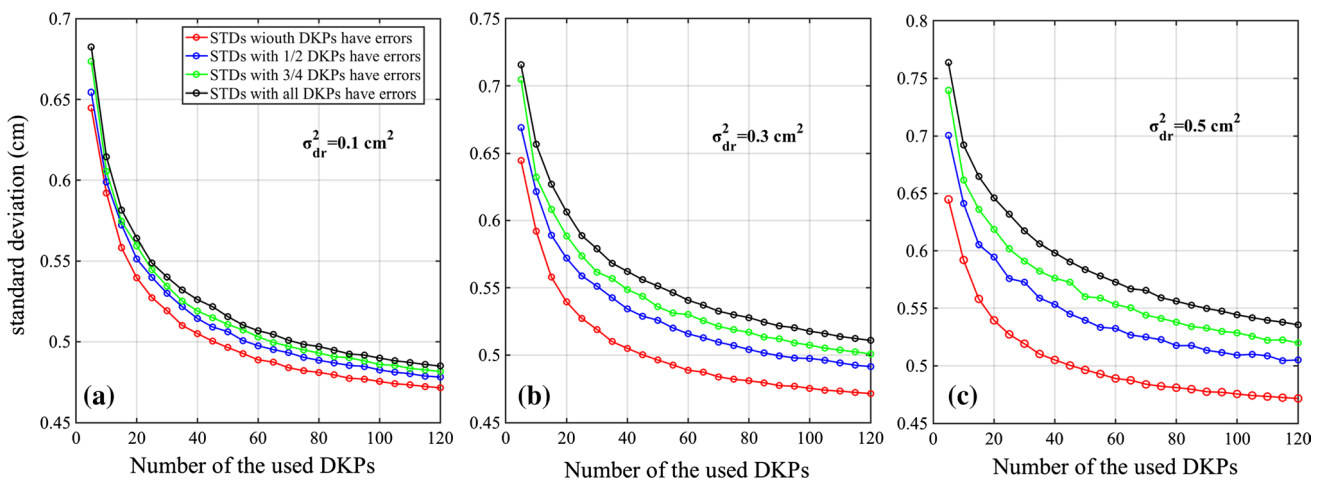


Fig. 20 Effects of the prior displacement errors on the MPD-InSAR-based results at pixel p_1 : **a** $\sigma_{d_r}^2 = 0.1 \text{ cm}^2$; **b** $\sigma_{d_r}^2 = 0.3 \text{ cm}^2$; **c** $\sigma_{d_r}^2 = 0.5 \text{ cm}^2$. $\sigma_{d_r}^2$ means the variance of those biased prior displacements. Red circles represent the MPD-InSAR results that no known

pixels have prior displacement errors. Green circles, blue circles and black circles denote the results that when 1/2, 3/4 and all of the known pixels have errors, respectively

5.4 Effects of possible un-compensated error components

In our method, we assume that the spatially correlated components of the observation errors are mainly caused by the turbulent atmospheric delays. In practice, the spatially correlated errors in an interferograms could be much more complicated than what we assumed, if some systematic errors or outliers were not completely compensated or calibrated. For example, the un-removed stratified atmospheric delays, possible residual orbital errors (the nonlinear components), DEM errors, unwrapping errors, and ionospheric phases (especially for long-wavelength SAR interferometry, e.g., L-band) can potentially exist in an interferograms and are spatially correlated too. However, the spatial stochastic properties of these components (e.g., residual orbital errors) are seldom or still not well studied till now. If these un-compensated components are spatially stationary and can be modeled by using a structure function based on the geostatistical method, then it is easy to conclude that they could be handled together with the turbulent atmosphere, and the proposed MPD-InSAR would still work fine for mitigating the effects of these components (all of the above spatial correlated components) in the reconstruction of the ground displacements. If these un-compensated components are non-stationary, no doubt, the performance of the proposed MPD-InSAR method would be affected to some degree, due to the incapability that the classical geostatistical method and structure function are used to model the non-stationary spatial random field. This, however, will be our future research topic.

6 Conclusions and outlooks

In this paper, we have presented a novel multiple phase difference-based InSAR approach (MPD-InSAR) to reconstruct the ground displacements by using multiple displacement-known pixels, and the number of that is only one for conventional InSAR, which is generally referred to as the reference pixel. In our method, a stochastic model of the MPD-InSAR measurements is considered and estimated pixel by pixel, and a minimum variance-based linear estimator was proposed to reconstruct the ground deformation. The new method is tested by using both the simulated datasets and the real Sentinel-1A data over Mexico City region, and the experimental results show that the MPD-InSAR approach can mitigate the atmospheric turbulence robustly, and the more displacement-known pixels we used, the more accurate the reconstructed deformations tend to be. Compared with the present tropospheric delay mitigation methods, our new method opens a new sight for mitigating the turbulent atmosphere effects, and this method can be implemented flexibly

no matter with or without external displacement dataset, and our method is also a good supplement for the present stratified atmosphere correction methods that cannot correct the effects of the turbulent atmosphere, like NWM-based methods, topography correlation-based methods.

Stochastic modeling for the MPD-derived displacements plays a key role in the MPD-InSAR approach. More accurate and reliable models for estimating the variance–covariance components of atmospheric delays and decorrelation noise may yield better results. In addition, possible errors due to the orbital errors, unwrapped errors, topography residuals also should be considered in practice. In this research, we only focus on the space domain (one interferogram); how to incorporate our method into time-series InSAR techniques would also be considered in our future researches.

Acknowledgements This work was partly supported by the National Key R&D Program of China (No. 2018YFC1503603) and a joint doctoral program of China Scholarship Council (201606370114). We would like to thank ESA (European Space Agency) for supplying the Sentinel-1A datasets through the WInSAR Projects. We also acknowledge JPL/Caltech for the use of ISCE software (Rosen et al. 2012) to generate our interferograms.

References

- Bamler R, Hartl P (1998) Synthetic aperture radar interferometry. *Inverse Prob* 14:R1–R54
- Bekaert DPS, Hooper A, Wright TJ (2015) A spatially variable power law tropospheric correction technique for InSAR data. *J Geophys Res Solid Earth* 120:1345–1356
- Berardino P, Fornaro G, Lanari R, Sansosti E (2002) A new algorithm for surface deformation monitoring based on small baseline differential SAR interferograms. *IEEE Trans Geosci Remote Sens* 40:2375–2383
- Cao Y-M, Li Z-W, Wei J-C, Zhan W-J, Zhu J-J, Wang C-C (2014) A novel method for determining the anisotropy of geophysical parameters: unit range variation increment (URVI). *Appl Geophys* 11:340–349
- Cao Y, Li Z, Wei J, Hu J, Duan M, Feng G (2017) Stochastic modeling for time series InSAR: with emphasis on atmospheric effects. *J Geodesy* 92:185–204
- Chen CW, Zebker HA (2000) Network approaches to two-dimensional phase unwrapping: intractability and two new algorithms. *JOSA A* 17:401–414
- Chen F, Guo H, Ma P, Lin H, Wang C, Ishwaran N, Hang P (2017) Radar interferometry offers new insights into threats to the Angkor site. *Science* 3:e1601284
- Cressie N (1990) The origins of kriging. *Math Geol* 22:239–252
- Ding XL, Li ZW, Zhu JJ, Feng GC, Long JP (2008) Atmospheric effects on InSAR measurements and their mitigation. *Sensors* 8:2231
- Elliott JR, Biggs J, Parsons B, Wright TJ (2008) InSAR slip rate determination on the Altyn Tagh Fault, northern Tibet, in the presence of topographically correlated atmospheric delays. *Geophys Res Lett* 35:L12309
- Emardson TR, Simons M, Webb FH (2003) Neutral atmospheric delay in interferometric synthetic aperture radar applications: statistical description and mitigation. *J Geophys Res Solid Earth* 108:2231
- Ferretti A, Prati C, Rocca F (2001) Permanent scatterers in SAR interferometry. *IEEE Trans Geosci Remote Sens* 39:8–20

- Foster J, Brooks B, Cherubini T, Shacat C, Businger S, Werner CL (2006) Mitigating atmospheric noise for InSAR using a high resolution weather model. *Geophys Res Lett* 33:L16304
- Gong W, Meyer FJ, Liu S, Hanssen RF (2015) Temporal filtering of InSAR data using statistical parameters from NWP models. *IEEE Trans Geosci Remote Sens* 53:4033–4044
- González PJ, Fernández J (2011) Error estimation in multitemporal InSAR deformation time series, with application to Lanzarote, Canary Islands. *J Geophys Res* 116:10404
- Hanssen RF (2001) Radar interferometry. Data interpretation and error analysis, vol 2. Springer, Netherlands
- Hooper A (2008) A multi-temporal InSAR method incorporating both persistent scatterer and small baseline approaches. *Geophys Res Lett* 35:L16302
- Jolivet R, Grandin R, Lasserre C, Doin MP, Peltzer G (2011) Systematic InSAR tropospheric phase delay corrections from global meteorological reanalysis data. *Geophys Res Lett* 38:L17311
- Jolivet R, Agram PS, Lin NY, Simons M, Doin M-P, Peltzer G, Li Z (2014) Improving InSAR geodesy using global atmospheric models. *J Geophys Res Solid Earth* 119:18
- Kaymaz I (2005) Application of kriging method to structural reliability problems. *Struct Saf* 27:133–151
- Kinoshita Y, Furuya M, Hobiger T, Ichikawa R (2012) Are numerical weather model outputs helpful to reduce tropospheric delay signals in InSAR data? *J Geodesy* 87:267–277
- Klein M (1967) A primal method for minimal cost flows with applications to the assignment and transportation problems. *Manag Sci* 14:205–220
- Knosp SH-G, Jónsson S (2010) Covariance estimation for dInSAR surface deformation measurements in the presence of anisotropic atmospheric noise. *IEEE Trans Geosci Remote Sens* 48:9
- Koziel S, Bekasiewicz A, Couckuyt I, Dhaene T (2014) Efficient multi-objective simulation-driven antenna design using co-kriging. *IEEE Trans Antennas Propag* 62:5900–5905
- Li Z (2005) Interferometric synthetic aperture radar (InSAR) atmospheric correction: GPS, moderate resolution imaging spectroradiometer (MODIS), and InSAR integration. *J Geophys Res* 110:B03410
- Li ZW, Ding XL, Liu GX (2004) Modeling atmospheric effects on InSAR with meteorological and continuous GPS observations: algorithms and some test results. *J Atmos Solar Terr Phys* 66:907–917
- Li ZW, Ding XL, Huang C, Zhu JJ, Chen YL (2008) Improved filtering parameter determination for the Goldstein radar interferogram filter. *ISPRS J Photogramm Remote Sens* 63:621–634
- Lin Y-NN, Simons M, Hetland EA, Muse P, DiCaprio C (2010) A multiscale approach to estimating topographically correlated propagation delays in radar interferograms. *Geochem Geophys Geosyst* 11:73
- López-Quiroz P, Doin M-P, Tupin F, Briole P, Nicolas J-M (2009) Time series analysis of Mexico City subsidence constrained by radar interferometry. *J Appl Geophys* 69:1–15
- Lu Z, Kwoun O, Rykhus R (2007) Interferometric synthetic aperture radar (InSAR): its past, present and future. *Photogramm Eng Remote Sens* 73:217–221
- Massonnet D, Feigl KL (1998) Radar interferometry and its application to changes in the Earth's surface. *Rev Geophys* 36:441–500
- Onn F (2006) Modeling water vapor using GPS with application to mitigating InSAR Atmospheric distortions. Ph.D dissertation, Stanford University
- Onn F, Zebker HA (2006) Correction for interferometric synthetic aperture radar atmospheric phase artifacts using time series of zenith wet delay observations from a GPS network. *J Geophys Res* 111:91020
- Osmanoğlu B, Dixon TH, Wdowinski S, Cabral-Cano E, Jiang Y (2011) Mexico City subsidence observed with persistent scatterer InSAR. *Int J Appl Earth Obs and Geoinf* 13:1–12
- Rockafellar RT (1993) Lagrange multipliers and optimality. *SIAM Rev* 35:183–238
- Rodriguez E, Martin JM (1992) Theory and design of interferometric synthetic aperture radars. *IEE Proc F (Radar Signal Process)* 139:147–159
- Rosen PA, Gurrula E, Sacco GF, Zebker H (2012) The InSAR scientific computing environment *EUSAR*. In: 9th European conference, pp 730–733
- Sudhaus H, Jónsson S (2009) Improved source modelling through combined use of InSAR and GPS under consideration of correlated data errors: application to the June 2000 Kleifarvatn earthquake, Iceland. *Geophys J Int* 176:389–404
- Wang Q, Shi W, Atkinson PM, Zhao Y (2015) Downscaling MODIS images with area-to-point regression kriging. *Remote Sens Environ* 166:191–204
- Xu WB, Li ZW, Ding XL, Zhu JJ (2011) Interpolating atmospheric water vapor delay by incorporating terrain elevation information. *J Geodesy* 85:555–564
- Yan Y, Doin M-P, Lopez-Quiroz P, Tupin F, Fruneau B, Pinel V et al (2012) Mexico City subsidence measured by InSAR time series: joint analysis using PS and SBAS approaches. *IEEE J Sel Topics Appl Earth Obs Remote Sens* 5:1312–1326
- Zebker H, Villasenor J (1992) Decorrelation in interferometric radar echoes. *IEEE Trans Geosci Remote Sens* 30:950–959
- Zebker HA, Rosen PA, Hensley S (1997) Atmospheric effects in interferometric synthetic aperture radar surface deformation and topographic maps. *J Geophys Res Solid Earth* 102:7547–7563